AGU ADVANCING EARTH AND SPACE SCIENCE

JGR Atmospheres

RESEARCH ARTICLE
10.1029/2020JD034255

Twice-Daily Monsoon Precipitation Maxima in the Himalayas Driven by Land Surface Effects

Hatsuki Fujinami[1], **Koji Fujita**[2], **Nobuhiro Takahashi**[1], **Tomonori Sato**[3], **Hironari Kanamori**[1], **Sojiro Sunako**[2,4], **and Rijan B. Kayastha**[5]

[1]Institute for Space-Earth Environmental Research, Nagoya University, Nagoya, Japan, [2]Graduate School of Environmental Studies, Nagoya University, Nagoya, Japan, [3]Faculty of Environmental Earth Science, Hokkaido University, Sapporo, Japan, [4]Now at Snow and Ice Research Center, National Research Institute for Earth Science and Disaster Resilience, Nagaoka, Japan, [5]Himalayan Cryosphere, Climate and Disaster Research Center, Department of Environmental Science and Engineering, School of Science, Kathmandu University, Dhulikhel, Nepal

Key Points:

- Twice-daily precipitation maxima, corresponding to day and night, occur widely across the Nepal Himalayas, including in the glacierized area
- A double band of rainfall that has twice-daily maxima exists over terrain at 500–1,000 and ~2,000 m asl on the southern slopes
- Upslope flows due to surface heating drive a daytime rainfall peak, and a monsoon nocturnal low-level jet likely creates a nighttime peak

Supporting Information:

Supporting Information may be found in the online version of this article.

Correspondence to:

H. Fujinami,
hatsuki@nagoya-u.jp

Citation:

Fujinami, H., Fujita, K., Takahashi, N., Sato, T., Kanamori, H., Sunako, S., & Kayastha, R. B. (2021). Twice-daily monsoon precipitation maxima in the Himalayas driven by land surface effects. *Journal of Geophysical Research: Atmospheres*, *126*, e2020JD034255. https://doi.org/10.1029/2020JD034255

Received 15 NOV 2020
Accepted 16 JUN 2021

Author Contributions:

Conceptualization: Hatsuki Fujinami, Tomonori Sato
Data curation: Koji Fujita, Hironari Kanamori, Sojiro Sunako, Rijan B. Kayastha
Formal analysis: Hatsuki Fujinami
Funding acquisition: Hatsuki Fujinami, Koji Fujita
Investigation: Hatsuki Fujinami, Koji Fujita, Nobuhiro Takahashi, Tomonori Sato, Hironari Kanamori
Resources: Rijan B. Kayastha
Supervision: Koji Fujita

Abstract

The diurnal cycle of precipitation is important to the hydroclimate in the Himalayas in summer; however, features of the diurnal cycle that affect precipitation from the foothills to glacierized, high-elevation areas are poorly understood. We investigated the diurnal cycle of precipitation using 3 years of in situ observations recorded close to a glacier at 4,806 m asl, and 17 years of data from the Tropical Rainfall Measuring Mission (TRMM) precipitation radar (PR) and the Integrated Multi-satellitE Retrieval for Global Precipitation Measurement (IMERG). The mechanisms that drive the diurnal cycle were examined using hourly European Center for Medium-Range Weather Forecasts Re-Analysis fifth generation (ERA5) data. In situ observations showed that the diurnal precipitation cycle has daytime and nighttime peaks, which both consist of high rainfall frequency and low rainfall intensity. In addition, twice-daily maxima exist in the TRMM PR data, particularly over two rain bands at around 500–1,000 m asl, and at ~2,000 m asl. Convective-type rainfall, with a lower rain-top height, occurs in the daytime, whereas stratiform-type rain, with a higher rain-top height, occurs at night, particularly over terrain at elevations above ~1,500 m asl. Land surface processes likely cause the two peaks in the diurnal cycle. Daytime surface heating drives upslope flows that promote condensation. At night, surface cooling over the plain to the south of the Himalayas causes low-level monsoon flows to accelerate, creating a nocturnal jet, which results in large-scale moisture flux convergence over the southern slopes.

Plain Language Summary

Orographically induced precipitation and meltwater from glaciers in the Himalayas feeds into the headwaters of major rivers such as the Indus, the Ganges, and the Brahmaputra, and provides water resources for the large population of South Asia. Glaciers from the central to the eastern Himalayas are sustained by summer precipitation, and the diurnal cycle is an important part of the climate system there. However, the features of the diurnal cycle, which stretches from the foothills to the glacierized high-elevation area in the Nepal Himalayas, are poorly understood. In this study, we investigated the diurnal cycle of precipitation in summer using data from 3 years of in situ observations (recorded close to a glacier at 4,806 m asl) and 17 years of space-borne precipitation radar observations. We identified twice-daily precipitation maxima, corresponding to daytime and nighttime peaks, in the diurnal cycle across much of the Nepal Himalayas. The two maxima are the result of different land surface effects. The daytime peak results from upslope flows that are driven by surface heating of the slopes, whereas the nighttime peak is caused by the acceleration of low-level monsoon flows toward the Himalayas as the surface cools over the plain to the south of the Himalayas.

1. Introduction

The hydrological cycle in the Himalayas is characterized by large amounts of precipitation over slopes and the existence of glaciers in high-elevation areas. The cycle maintains the headwaters of major rivers such as the Indus, the Ganges, and the Brahmaputra, and provides water resources for South Asia's large population (Immerzeel et al., 2010). Changes to the hydrological cycle in the Himalayas can affect global sea level through glacier mass loss, and may thus also affect the global hydrological cycle under future climate-change scenarios (Marzeion et al., 2020).

Writing – original draft: Hatsuki Fujinami

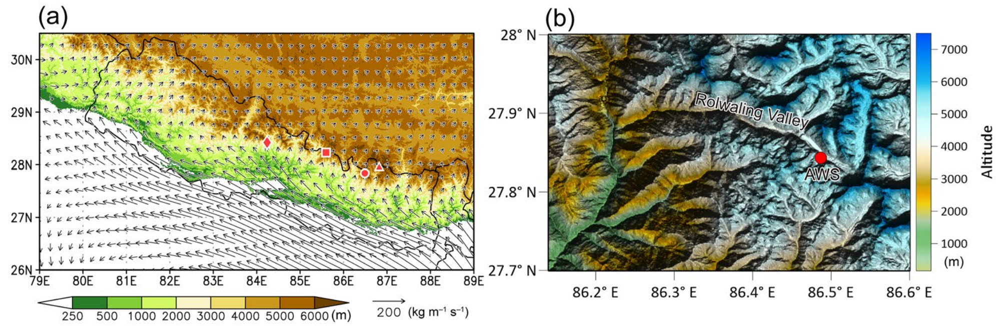

Figure 1. (a) Topography (shading) and climatological mean (1998–2014) vertically integrated water-vapor flux (vectors) in summer (June–September) around Nepal. The topography comes from the Global Multiresolution Terrain Elevation Data 2010 (GMTED2010) product, developed collaboratively by the United States Geological Survey (USGS) and the National Geospatial-Intelligence Agency (NGA). (b) As in (a), but for the Rolwaling Valley and without the water-vapor flux vectors; (b) was produced from the Advanced Space-borne Thermal Emission and Reflection Radiometer (ASTER) Global Digital Elevation Model Version 3 (GDEM3) product, developed collaboratively by National Aeronautics and Space Administration (NASA) and Japan's Ministry of Economy, Trade, and Industry (METI). The red circles in (a) and (b) mark the location of the automatic weather station (AWS) in Rolwaling Valley, in the eastern Nepal Himalaya. The square, triangle, and diamond in (a) mark the locations of rain gauges at Yala Glacier, Langtang Valley, and Pyramid Station, near a glacier in the Khumbu Valley, and at Rambrong, in the Marsyandi River basin, respectively. See the text for rain gauge stations.

In boreal summer, the Asian monsoon circulation system becomes established and southeasterly winds blow toward the Himalayas (Figure 1), carrying warm, humid air masses from the South Asian monsoon and creating conditions that are favorable for orographically induced precipitation over the Himalayan slopes. The Himalayas themselves significantly influence the South Asian monsoon circulation system through the effects of orographic insulation (Boos & Kuang, 2010).

The hydrological cycle differs from the western to the eastern Himalayas. In the central-eastern Himalayas, most of the total annual precipitation falls in summer (Bookhagen, 2010; Salerno et al., 2015; Shea et al., 2015; Yang et al., 2018), which makes summer precipitation a crucial part of the high-elevation hydroclimate in the Nepal Himalayas (i.e., the central Himalayas), including for glacier mass balance (Sakai & Fujita, 2017). Observations from the Tropical Rainfall Measuring Mission (TRMM) precipitation radar (PR), which operated continuously from 1998 to 2014, provide useful information about summer precipitation around the Himalayas, including detailed information about the spatial distribution and vertical structure of precipitation systems, and their topographic dependency (Barros et al., 2004; Bhatt & Nakamura, 2005, 2006; Bookhagen & Burbank, 2006; Fu et al., 2018; Houze et al., 2007; Medina et al., 2010; Shrestha et al., 2012). There are two peaks in the spatial distribution of summer (June–August) precipitation over southern slopes in the Nepal Himalayas, and these are oriented along the strike directions. The peaks are associated with the two-step topography, which comprises the Sub-Himalayas at 500–1,000 m above sea level (asl), and the Lesser Himalayas at ~2,000 m asl (Bookhagen & Burbank, 2006; Shrestha et al., 2012). The peak over the Sub-Himalayas represents strong convective-type rainfall, whereas the peak over the Lesser Himalayas corresponds to frequent, but less intense, stratiform-type rainfall.

Meteorological observations at elevations of >4,000 m asl over the Himalayas are still extremely scarce (Shea et al., 2015). Therefore, in situ observations with high temporal resolution remain essential for a basic understanding of meteorological data in such areas, and to obtain true surface data for remote sensing observations from space (Barros et al., 2000, 2004; Salerno et al., 2015; Shea et al., 2015; Ueno et al., 2001, 2008; Yang et al., 2018). The diurnal cycle constitutes the building blocks that form the hydrological cycle in mountainous regions. In situ measurements from automatic weather stations (AWSs) located on and around Yala glacier in Langtang Valley, central Nepal Himalayas, at 4,831, 4,919, and 5,090 m asl show that the diurnal cycle of summer precipitation has two peaks, which correspond to daytime and nighttime (Shea et al., 2015). A similar feature can be seen in observations from a weather station at Rambrong at 4,400 m asl and other stations above 2,100 m asl in the Marsyandi river basin in the central Nepal Himalayas (Barros et al., 2000), and from the Pyramid Station at 5,035 m asl in Khumbu Valley in the eastern Nepal Himalayas

(Ueno et al. 2008; Yang et al., 2018), and from five surface stations at altitudes ranging from 3,341 to 4,321 m asl along a valley in the Himalayas at around 89°E (Ouyang et al., 2020). In contrast, in situ observations made at 3,570, 3,833, and 4,260 m asl in Khumbu Valley, and at Khudi at 780 m asl and other stations below 1,500 m asl in the Marsyandi river basin, show a single peak for precipitation, which corresponds to nighttime (Barros et al., 2000; Ueno et al., 2001, 2008; Yang et al., 2018).

In general, daytime precipitation results from thermally induced upslope air flow (anabatic slope flow) that is driven by surface heating during the day (Potter et al., 2018). Upslope flows move moist air to higher altitudes as the ground elevation increases, and condensation therefore occurs over the slopes (Bhatt & Nakamura, 2006; Kurosaki & Kimura, 2002; Ohsawa et al., 2001; Ouyang et al., 2020; Shrestha et al., 2012; Ueno et al., 2008; Yang et al., 2018). In contrast, precipitation is more frequent during the night over the foothills of the Himalayas and over the southern slopes of the Meghalaya Plateau (Bhatt & Nakamura, 2006; Fujinami et al., 2017; Hirose et al., 2008). Bhatt and Nakamura (2006) proposed that downslope flows (gravity currents) driven by nighttime precipitation at higher elevations enhance nocturnal moist convection over the Himalayas, and that this convection is enhanced by cloud-top radiative cooling. Fujinami et al. (2017) described the detailed diurnal cycle of precipitation around the Meghalaya Plateau in northeastern India, to the south of the Himalayas, using diurnal (hourly) climatology based on TRMM PR data with high spatial resolution. Low-level, southerly monsoon flow with a jet-like structure intrudes the land-covered area from the Bay of Bengal. The strength and vertical structure of the low-level flows are strongly affected by atmospheric boundary layer processes over the land, particularly by the nocturnal acceleration and daytime deceleration of low-level southerly winds. Low-level convergence is enhanced by the nocturnal acceleration of the low-level jet (i.e., the nocturnal jet), which results in a nocturnal maximum for precipitation over the southern slopes of the Meghalaya Plateau. Note that onshore southerly flows may also reach the Himalayas (Figure 1). Chen (2020) used 3-h precipitation and 6-h atmospheric reanalysis data sets to highlight the relationship between nocturnal precipitation over the foothills of the Himalayas and the nocturnal low-level jet.

The diurnal cycle of precipitation and how it changes from the foothills through to areas of high elevation is poorly understood, and its driving mechanisms remain unknown. To improve our understanding of meteorology in high-elevation areas, and of how it relates to glaciers, it is important to understand the mechanisms that drive precipitation variability in glacier catchment areas, and it is particularly important to understand the diurnal cycle. In this study, we first present evidence for the diurnal cycle of precipitation using hourly observations recorded at an AWS at 4,806 m asl in the Rolwaling Valley in the eastern Nepal Himalayas. We then use accumulated diurnal (hourly) climatology from TRMM PR data with high spatial resolution to show how the diurnal cycle varies spatially across the Nepal Himalayas, and how precipitation varies with altitude over the rising slopes. We propose a mechanism that may drive the diurnal cycles over the Himalayas by considering hourly atmospheric reanalysis data, focusing particularly on the effects of land-atmosphere interactions. In this study, we consider spatial scales sufficient to cover the entire Nepal Himalayas and South Asian monsoon domain, rather than determining mechanisms that are effective over regional scales of less than ∼10 km.

2. Data and Methods

2.1. In Situ Observations

We used in situ observation data recorded at 4,806 m asl in the Rolwaling Valley in the eastern Nepal Himalayas (Figure 1b; Fujita et al., 2021). In May 2016, an AWS was installed close to the terminal of Trakarding Glacier and Tsho Rolpa Lake, the largest glacial lake in Nepal, to investigate glacier mass balance (Sunako et al., 2019). Precipitation was measured using a tipping-bucket rain gauge with 0.1 mm resolution. Hourly precipitation is the total precipitation amount of the preceding hour. The AWS also recorded other standard meteorological elements, including air temperature, relative humidity, wind speed, and direction, and radiation. Detailed information on the AWS is provided in Sunako et al. (2019). The hourly air temperature (i.e., mean temperature of the preceding hour) is always greater than 0°C during summer (June–September; figure not shown), and summer precipitation therefore falls as rain at the AWS. We used data from three summers: 2016, 2017, and 2018. There are no values missing during the analysis periods. Considering multiyear data is useful for determining what is typical and common for the diurnal cycle of precipitation and other meteorological variables in the glacierized high-elevation area in the central Himalayas.

We calculated hourly means and standard deviations for each local time to show the robustness of the 3-year mean diurnal cycles of air temperature, relative humidity, solar radiation, wind speed, and direction. We calculated the lower (25 percentile) and upper (75 percentile) quartiles for hourly precipitation. Seasonal mean diurnal cycles of rainfall rate were calculated using all data at each local time, irrespective of whether or not it was raining (i.e., unconditional rain rate).

2.2. TRMM PR

We used TRMM PR 2A25 version 7 data (Iguchi et al., 2000) for 17 summers (1998–2014) to examine the long-term mean properties and diurnal cycle of precipitation over slopes in the Nepal Himalayas. The TRMM satellite has a nonsun-synchronous orbit and can observe three-dimensional structures of precipitation systems at all local times. Therefore, the accumulation of instantaneous precipitation properties in long-term periods can provide accurate statistics (i.e., climatology) for their diurnal cycles (Hirose et al., 2017a). The PR is an active phased-array system operating in the Ku band (13.8 GHz). The minimum rainfall rate that the PR can detect is ~0.7 mm h^{-1} (Kummerow et al., 1998). The original horizontal resolution was 4.3 km at nadir but was increased to 5.0 km after an orbital-boost maneuver in 2001. We used the near-surface rainfall rate to examine the spatial distribution of rainfall and to calculate rainfall frequency (the number of rainfall events as a percentage of the total number of observations from a grid for TRMM PR observation) and conditional rain rate (the mean near-surface rainfall rate during rain events). We used the rain flag from the TRMM PR product, 2A25, to classify samples as rain. The PR algorithm classifies rain pixels into three categories: convective, stratiform, and other. Storm-height data were also used to examine convection characteristics, such as depth. We remapped all data from each individual swath to a regular grid with spacing of 0.05° in both longitude and latitude, which is equivalent to the PR footprint. The gridded data were then averaged for each local time during June–September over all years to produce summer mean diurnal (hourly) climatologies of precipitation properties. The hourly data are the mean value of the preceding hour. All variables from TRMM PR were smoothed as 3-h running means to reduce sampling errors. Precipitation was generally underestimated in the TRMM PR data, relative to the rain gauge observations made over land (Bookhagen & Burbank, 2006; Fujinami et al., 2017; Terao et al., 2017), but the TRMM PR data did successfully capture the fine-scale spatial distribution for precipitation, which depends on topographic features (Biasutti et al. 2012; Bookhagen & Burbank, 2006; Fujinami et al. 2017; Hirose et al., 2008, 2017b).

The Global Precipitation Measurement (GPM) core observatory supersedes the TRMM mission which ended in 2014. The space-borne GPM observatory carries a dual-frequency phased-array precipitation radar (DPR), operating in the Ku and Ka bands (13.6 and 35.5 GHz, respectively). The DPR is sensitive to light precipitation intensities, down to around 0.2 mm h^{-1}, which may be effective for observing precipitation over high-elevation areas. Unfortunately, the lower frequency of the GPM observations than that of TRMM means that they cannot be used to construct a climatological mean diurnal cycle at present. Therefore, we used TRMM PR diurnal climatology in the preset study.

We applied cluster analysis to objectively classify patterns in the diurnal cycle of precipitation frequency based on TRMM PR diurnal climatology and to show their spatial distribution over the Nepal Himalayas. Ward's method was applied to the data (Wilks, 2011); this is a widely used hierarchical clustering method that does not operate on the distance matrix. Seven subjectively chosen clusters well capture regional features of the diurnal cycle derived from TRMM PR data.

2.3. IMERG

We also used the Integrated Multi-satellitE Retrievals for GPM (IMERG) V06 B Level 3 final run precipitation product, complementary to TRMM PR, which was provided on a 0.1° × 0.1° horizontal grid with 30-min temporal resolution (Huffman et al., 2019; Tan et al., 2019). The variable name used is "precipitationCal." The data may also aid the understanding of diurnal cycles based on studies of in situ observations. We used data for the period 2000–2014, corresponding to the TRMM era. The IMERG uses precipitation estimates derived from passive microwave radiometer (MWR) data using as many low-Earth-orbit satellites as possible. The best TRMM and GPM estimates of precipitation were used as calibration standards: the GPM Combined Radar-Radiometer algorithm using GPM Microwave Imager (GMI) and DPR during the GPM era (2014–present; CORRA-G), and an equivalent computation using a TRMM Microwave Imager (TMI) and PR during the TRMM era (1998–2014; CORRA-T), collectively referred to as CORRA. The IMERG algorithm combines CORRA and the other passive microwave data with microwave-calibrated infrared (IR) geosynchronous-orbit satellite and monthly data from the Global Precipitation Climatology Center to estimate precipitation (Huffman et al., 2019). Data were averaged over consecutive 30-min periods during June–September for all years to produce summer mean diurnal (30 min) climatology.

2.4. Comparison and Validation of Rainfall Data Sets

Active microwave sensors such as TRMM PR have an advantage in detecting fine-scale features of precipitation around mountains because retrievals are less sensitive to the background environment than those of passive MWR or infrared radiometers (Hirose et al., 2017b). However, TRMM PR has a minimum detectable rain rate of ~0.7 mm h^{-1}. At higher elevations, the rain rate can be less than this threshold because of low water-vapor conditions. In contrast, the Goddard profiling algorism (GPROF) estimates have thresholds of 0.03 mm h^{-1}, as employed in IMERG to retrieve precipitation rate (Huffman et al., 2020). The MWR algorithms used for estimating rainfall rate over land are based on the scattering effect of solid hydrometeors above the freezing level, in the high-frequency channels. However, in high-elevation areas such as the Himalayas, the microwave estimates are replaced with IR estimates over snowy/icy surfaces (Huffman et al., 2020). Either way, IMERG may be able to retrieve precipitation at higher elevations if there are precipitating clouds of high cloud-top height. A comparison of the precipitation reported by the two different products may provide insights into the properties of precipitation across the mountain slopes, since the products may have different sensitivities to vertical structure and specific stages in the evolution of a precipitation system (Yamamoto et al., 2011, 2017).

It is not easy to directly compare diurnal cycles of precipitation among in situ data and satellite-derived precipitation data sets because of problems such as the spatial representativeness of one-point rain gauge measurements, the footprint size of precipitation radar, and the grid size of data. Most in situ precipitation data are for single or a few years. In contrast, TRMM PR provides diurnal climatology from the accumulation swath data. We attempted to compare features of diurnal cycles in terms of frequency and value of precipitation maxima for previous in situ measurements, and TRMM PR and IMERG diurnal climatologies. We referenced the results from in situ observation networks (Barros et al., 2000, 2004) over the summers of 1999 and 2000 from elevations of 510 m to 4,400 m asl in the Marshandi River Basin in the central Nepal Himalayas (Figure 1 in the present study and Barros et al., 2000). Latitude-local time cross-sections in summer precipitation based on TRMM PR and IMERG at longitudes closely corresponding to the observation network are shown in Figure S1. TRMM PR can capture two maxima in the afternoon and at nighttime above ~1,000 m asl, whereas only nighttime maximum appears below ~1,000 m. Maximum values range from 1 to 2 mm h^{-1} (Figure S1b), which is generally consistent with the results of Barros et al. (2000, 2004). In contrast, the precipitation rate tends to be lower above 3,000 m asl relative to in situ measurements. Therefore, TRMM PR can generally capture the observed diurnal pattern of precipitation in the region and is applicable to the Nepal Himalayas. IMERG exhibits a single nighttime peak only in the area shown in Figure S1c, with no daytime precipitation peak above 1,000 m. Higher rainfall rates are estimated above 3,000 m asl during nighttime than with TRMM PR. Further discussions of the comparison, particularly with regard to higher elevations, are provided in Section 3.1.

2.5. ERA5 Reanalysis

We used hourly European Center for Medium-Range Weather Forecasts ReAnalysis fifth generation (ERA5) data on a 0.25° × 0.25° grid for the period covered by the TRMM PR data (Hersbach et al., 2020). ERA5 provides high-quality global data for atmospheric circulation and land surface parameters such as surface heat fluxes (Martens et al., 2020). The data were very useful here in examining land-atmosphere interactions in terms of explaining diurnal cycles. The high spatiotemporal resolution of this data set also allows us to examine detailed features of the diurnal cycles of meteorological variables around the Himalayas more easily than would be possible using only the 6-h and coarse-grid reanalysis data. The overall slope gradient in the Himalayas in ERA5 is similar to that of the actual topography. However, local topography (<30 km in the horizontal scale) cannot be resolved even by fine-scale reanalysis. Therefore, it cannot reproduce local-scale mountain-valley circulation. Moreover, upper-air sounding data assimilated in the reanalysis are scarce over the Himalayas and Tibetan Plateau. Therefore, atmospheric circulation and its variability around the Himalayas in ERA5 reanalysis may be strongly influenced by the performance of the numerical model employed in ERA5. Nevertheless, fine spatiotemporal reanalysis can provide useful insights into the mechanisms that drive diurnal variations around the Himalayas, as shown in Section 3.2. Zonal wind, meridional wind, specific humidity, air temperature, vertical velocity, and surface sensible heat flux were used in this study. Potential temperature and equivalent potential temperature were calculated from air temperature and specific humidity (Bolton, 1980). The vertically integrated water-vapor flux from the surface to 100 hPa was calculated from the zonal wind, meridional wind, and specific humidity. Hourly data were used to construct a composite diurnal cycle (or other temporal pattern) for meteorological variables related to the diurnal cycle of precipitation.

We used the unified local time (LT; UTC + 6 h) at 90°E instead of Nepal Standard Time (UTC + 5 h 45 m), because the ERA5 and gridded TRMM PR data are provided in UTC time coordinates. Throughout this paper, the axis for time in the diurnal cycle starts from 06:00 LT (i.e., approximately sunrise) instead of 00:00 LT. This makes precipitation peaks clear, including during nighttime, and enables a consideration of their driving mechanisms because the peaks are largely associated with the development of the atmospheric boundary layer owing to radiative heating and cooling of the surface.

3. Results

3.1. Bimodal Diurnal Cycle of Precipitation

3.1.1. In Situ Observations

We used in situ meteorological observations recorded at the AWS at 4,806 m asl to assess the properties of precipitation over a high-elevation area with a glacier (Figure 1b).

Figures 2a, 2c and 2e show how the precipitation measured at the AWS varied over 24-h periods, and how this changed through the summer in 2016, 2017, and 2018. This allowed us to examine the diurnal cycle of the AWS-measured precipitation, and to assess its seasonal variation. The total June–September precipitation was 603 mm in 2016, 513 mm in 2017, and 468 mm in 2018. In July and August in all 3 years, most precipitation occurred between 12:00 and 05:00 LT the following day, and there was a period around 20:00 LT when precipitation was suppressed, although the start and end dates for the period of continuous precipitation (the rainy season) differed from year to year (Figures 2b, 2d and 2f). Most precipitation during the summer was weak. Precipitation events with rainfall rates of ≤0.5 mm h^{-1} accounted for 63% of all precipitation events in 2016, 66% of events in 2017, and 69% of events in 2018 (Figures 2g–2i). More than 80% of the total precipitation fell with an intensity less than 1.0 mm h^{-1}. Higher-intensity precipitation (>1.5 mm h^{-1}) occurred intermittently, and rarely persisted for more than 3 h.

In all 3 years, the mean diurnal cycle of summer precipitation included double peaks of both precipitation rate and precipitation frequency, corresponding to daytime (13:00–18:00 LT) and nighttime (23:00–04:00 LT; Figure 3). Precipitation frequency is calculated for each hour as the number of days for which precipitation measured for that hour during summer exceeded 0.1 mm, and is expressed as a percentage of the total number of observations available for that hour in summer that year (122). Precipitation amounts at the two peaks are almost the same for all 3 years. The diurnal cycle of precipitation frequency is similar to that of precipitation amount, and peaks at ∼50% at the two maxima. The precipitation frequency determines the shape of the diurnal cycle of precipitation.

The surface meteorological variables show features that are related to the two precipitation peaks. The 3-year mean diurnal cycle of precipitation is characterized by a minimum at 10:00 LT, by two maxima at around 14:00–16:00 and 00:00–02:00 LT, and by a break in precipitation at around 20:00 LT (Figure 4a). Incoming solar radiation warms the surface after sunrise, causing the surface air temperature to rise (Figure 4b). The warmed slope surface induces west-northwesterly or northwesterly upvalley flows in the Rolwaling Valley from 12:00 to 17:00 LT, with a peak wind speed that exceeds 2.5 m s^{-1} at 13:00–14:00 LT (Figure 4c). These upvalley flows carry moist air along the valley that cools adiabatically as it travels up the slope, promoting condensation. A high relative humidity of around 95% and weak southerlies with wind

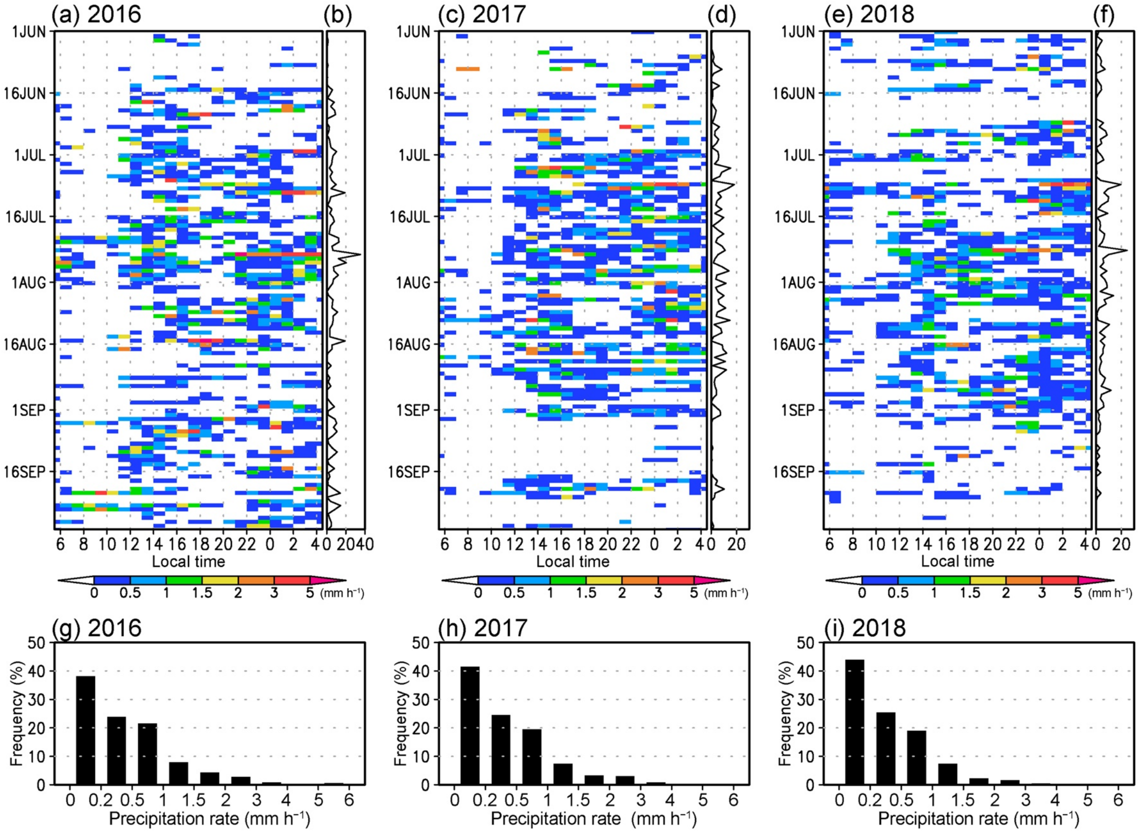

Figure 2. Hourly precipitation observed at the Rolwaling automatic weather station (AWS) for summer (June–September), shown by date and local time for (a) 2016, (c) 2017, and (e) 2018. Time series of daily total precipitation (mm day^{-1}), defined as the total precipitation from 06:00LT to 05:00LT of the following day, for (b) 2016, (d) 2017, and (f) 2018. Note that the axis range is different in (b), (d), and (f). Frequency distribution for hourly precipitation (mm h^{-1}) in (g) 2016, (h) 2017, and (i) 2018. The *y*-axis values in (g–i) are the number of precipitation events, expressed as a percentage of the total number of summer precipitation events for that year.

speeds less than 1 m s^{-1} were observed around the time of the nighttime precipitation peak, indicating that the surface air was almost saturated at this time. However, the surface meteorological variables do not explain why precipitation reaches a maximum in the middle of the night, which suggests that a change in large-scale atmospheric circulation may be responsible for the nighttime precipitation peak, rather than a change in the surface meteorological variables.

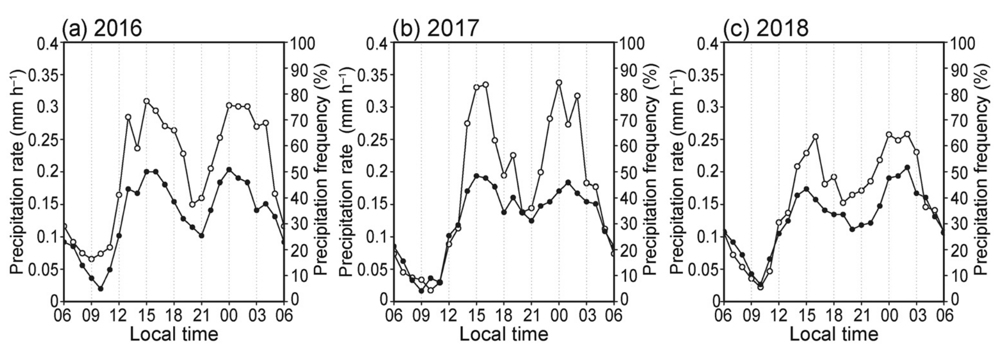

Figure 3. Mean diurnal cycles of precipitation (mm h^{-1}; line with open circles) and precipitation frequency (%; line with closed circles) in summer (June–September) at the Rolwaling automatic weather station: (a) 2016, (b) 2017, and (c) 2018.

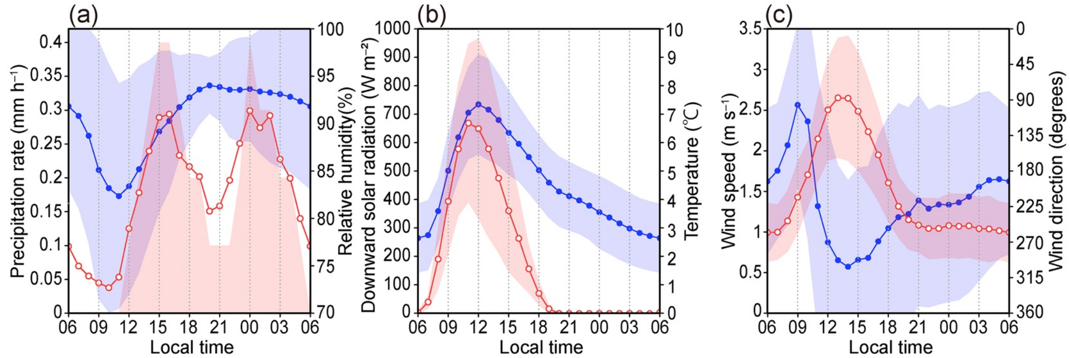

Figure 4. Three-year (2016, 2017, and 2018) mean diurnal cycles of variables measured during summer (June–September) at the Rolwaling automatic weather station: (a) Unconditional precipitation rate (mm h^{-1}; red line with open circles) and relative humidity (%; blue line with closed circles); (b) Downward shortwave radiation (W m^{-2}; red line with open circles) and surface air temperature (°C; blue line with closed circles); and (c) wind speed (m s^{-1}; red line with open circles) and wind direction (degrees from North (0 = northerlies), blue line with closed circles). Shadings in precipitation indicate the range between lower (25 percentile) and upper (75 percentile) quartiles, and ±1 standard deviation for other variables.

Our results provide evidence for twice-daily precipitation maxima over the high-elevation glacierized area from multiyear observations. The observational evidence from our study, and evidence of similar diurnal cycles presented in previous studies (Barros et al., 2000, 2004; Ouyang et al., 2020; Shea et al., 2015; Ueno et al. 2008; Yang et al., 2018), suggests that the double diurnal peaks of precipitation are probably common to high-elevation areas in the Nepal Himalayas.

3.1.2. Diurnal Cycles Across the Nepal Himalayas

To investigate the relationship between the precipitation peaks observed at the AWS in Rolwaling Valley and the distribution of precipitation, we show the spatial distribution of precipitation across the Nepal Himalayas in the TRMM PR and IMERG data in Figure 5. The minimum precipitation at the Rolwaling AWS was 0.05 mm h^{-1}, which occurred between 08:00 and 11:00 LT. At this time, precipitation amount is large over elevations of less than 500 m asl in the foothills of the Himalayas, along Nepal's national border (Figures 5a and 5d). The same patterns appear in the spatial distribution for precipitation in the TRMM PR and IMERG data sets. Precipitation in the grid cell closest to the AWS is 0.1 mm h^{-1} in the TRMM PR data, and 0.11 mm h^{-1} in the IMERG product. The AWS recorded a daytime peak in precipitation of 0.26 mm h^{-1} between 14:00 and 17:00 LT, at which point there is a double band of rainfall that falls on ground at ∼500 and ∼2,000 m asl on the southern slopes of the Himalayas in the TRMM PR data (Figure 5b). This spatial distribution is structurally similar to the mean June–August distribution presented in Shrestha et al. (2012). In contrast, the two rainbands are not present in the IMERG data. This difference between the two products suggests that the daytime precipitation system is low in height and small in horizontal scale (i.e., convective-type precipitation), because the IMERG precipitation estimates are highly sensitive to information from infrared data. Precipitation estimates for the grid cell closest to the AWS in the TRMM PR and IMERG data are 0.08 and 0.24 mm h^{-1}, respectively. Values in the TRMM PR data are much smaller than the in situ observations recorded at the AWS. The nighttime precipitation peak of 0.28 mm h^{-1} occurred between 00:00 and 02:00 LT at the AWS, at which time the TRMM PR and IMERG data are dominated by a rainband at higher elevations (>1,500 m asl). The rainband is indicative of higher cloud-top heights and a wider precipitation system (i.e., stratiform-type precipitation), compared with daytime conditions; however, precipitation amounts at the grid cell closest to the AWS in the TRMM PR and IMERG data at this time are 0.09 and 0.48 mm h^{-1}, respectively. Precipitation around the AWS is not detected in the TRMM PR product (Figures 5a–5c). In fact, the number of precipitation events in the Rolwaling Valley in the TRMM PR product over the 17 summers considered in this study is too small to construct a climatological mean diurnal cycle (53 events are detected from a total of 1530 summer TRMM PR observations for the grid cell closest to the AWS). In contrast, the IMERG rainfall amount of 0.48 mm h^{-1} at the AWS location is an overestimate, relative to the 3-year mean of the precipitation observations at the AWS, which was 0.28 mm h^{-1}. The comparison of the diurnal precipitation cycles among the three data sets is shown in Figure S2. Rainfall

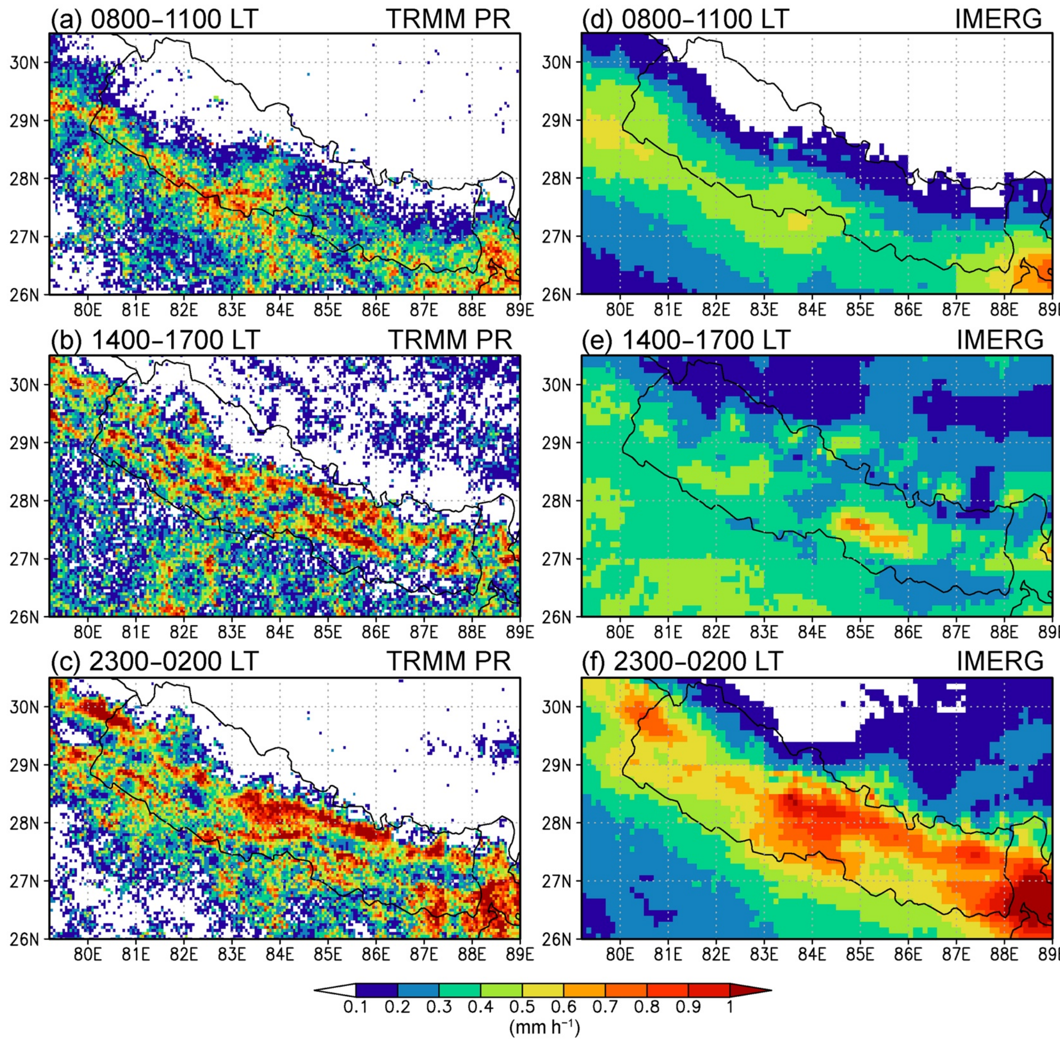

Figure 5. Composites of precipitation in the Tropical Rainfall Measuring Mission (TRMM) precipitation radar (PR) data for (a) 08:00–11:00 LT (02:00–05:00 UTC), (b) 14:00–17:00 LT (08:00–11:00 UTC), and (c) 23:00–02:00 LT (17:00–20:00 UTC) in summer (June–September) for 1998–2014 (17 years). LT is local time at 90°E. (d–f) As in (a–c), but for precipitation in the Integrated Multi-satellitE Retrieval for Global Precipitation Measurement (IMERG) data.

rate from TRMM PR shows significant underestimation compared with that from the AWS, except in the early morning, although it seems to show two weak peaks in daytime and nighttime, and the rainfall rate from IMERG shows a single nighttime peak with overestimation during nighttime. Note that the IMERG product detected precipitation that was part of a rainband that developed during the night over terrain above 4,000 m asl. This means that there were patterns of cloud cover that brought precipitation to the AWS location during the night.

Figure 5 shows that the TRMM PR product may struggle to capture precipitation over the high-altitude areas of the Himalayas, where the elevation exceeds around 4,000 m asl. However, precipitation over terrain at altitudes below around 4,000 m asl is captured more reasonably in the TRMM PR data than in the IMERG data, as in the results shown in Figure S1. We present results here from the cluster analysis of the diurnal cycle of rainfall frequency in the TRMM PR data, to investigate whether the twice-daily maxima are features unique to glacierized high-elevation areas, such as where the Trakarding and Yala glaciers are located, or whether these maxima occur in other areas of the Nepal Himalayas. Note that the TRMM PR footprint is ~5 km, so the spatial distribution of the clusters may not capture spatial information at scales smaller than 5–10 km. This means that Figure 6b does not reflect diurnal signals that are related to narrow

10.1029/2020JD034255

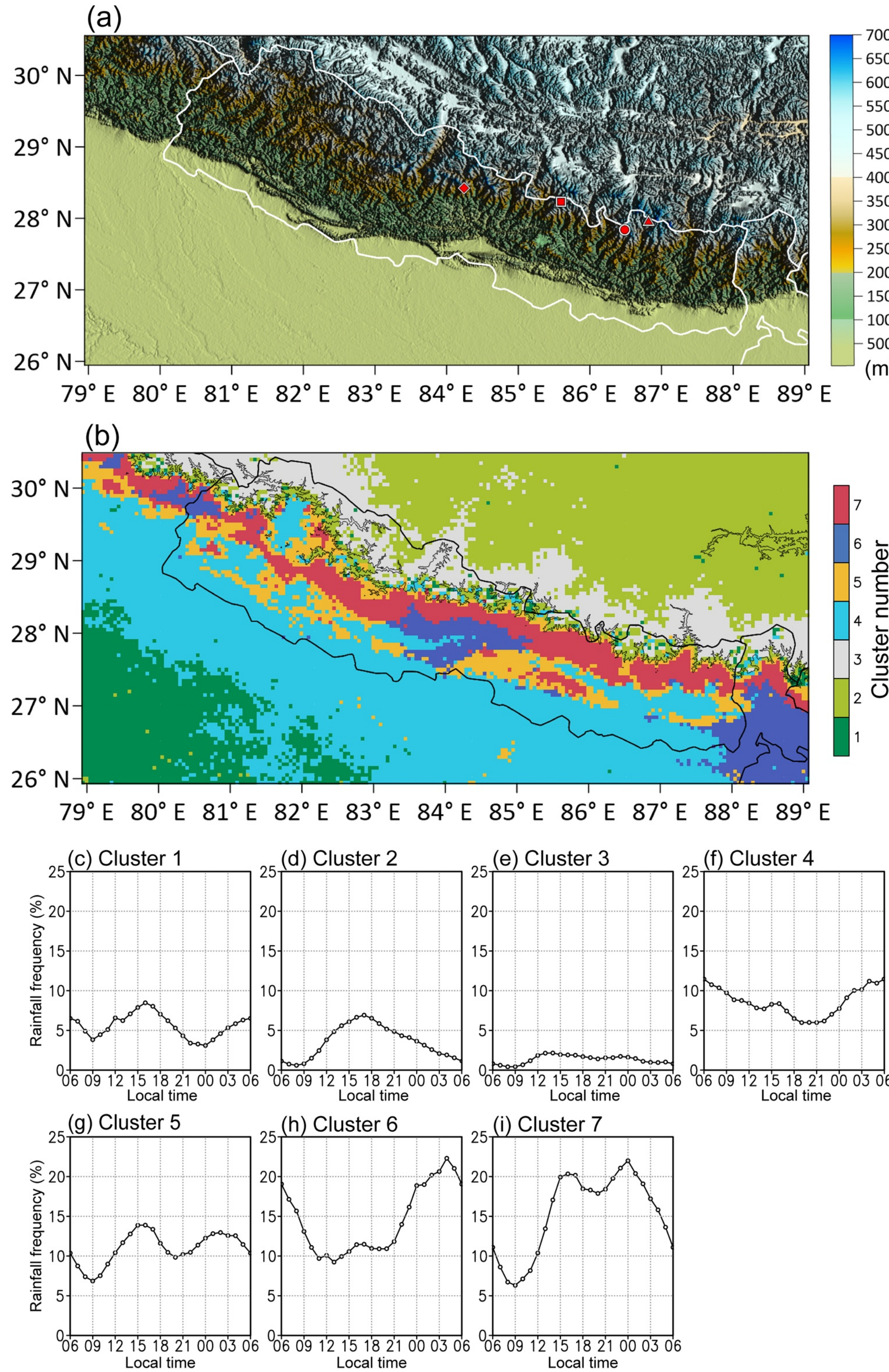

Figure 6. (a) Relief map of Nepal (from GMTED2010 data). The circle, triangle, square, and diamond mark the locations of the Rolwaling automatic weather station (AWS), Yala Glacier AWS, Pyramid Station, and Rambrong rain gauge station, respectively. See the text for the AWSs. (b) Spatial distribution of the seven clusters of the diurnal cycle in precipitation frequency, calculated from the Tropical Rainfall Measuring Mission (TRMM) precipitation radar (PR) data. Thin solid lines are topographic contours at 4,000 m. Lower panels (c–i): the mean diurnal cycle of precipitation frequency in: (c) cluster 1, (d) cluster 2, (e) cluster 3, (f) cluster 4, (g) cluster 5, (h) cluster 6, and (i) cluster 7.

valleys, or to ridges that are less than ~10 km wide. One striking feature in the cluster analysis results is a band of high-frequency precipitation with peaks at 16:00 and 00:00 LT, consistent with the peaks in the Rolwaling AWS (Figure 4a), which are classified as cluster 7 (Figures 6b and 6i). This corresponds to the band of high rainfall that was observed in the daytime and nighttime over areas at around 2,000 m asl (Figures 5b and 5c). The area occupied by cluster 7 is surrounded by an area classified as cluster 5, which also has a bimodal diurnal cycle, although the rainfall frequency is lower than for cluster 7 (Figure 6g). Cluster 5 also appears at around 500 m asl. Below 500 m asl, the diurnal cycle has a single peak, which occurs at 06:00 LT (cluster 4, Figure 6f). There is a midnight-to-early morning peak in the diurnal precipitation cycle over areas between 500 and 2,000 m asl in central Nepal, and over the area between 88°E and 89°E in India, and the rainfall frequency is high in these areas (cluster 6, Figure 6h). Precipitation for most grid cells over areas at elevations of >4,000 m asl (thin contour in Figure 6b) in the Nepal Himalayas is categorized into clusters 2 and 3 (Figures 6d and 6e), including precipitation for the grid cells that are closest to the AWSs at the Trakarding Glacier, the Yala Glacier, and the Pyramid Station. Precipitation frequency for these cells is much lower than that recorded at the AWSs (Figure 3 in this study and Figure 8 in Shea et al., 2015). Precipitation over the Tibetan Plateau to the north of the Himalayas is characterized by an afternoon peak (Figure 6d), similar to the findings presented in other studies (Fujinami et al., 2005; Hirose et al., 2008). The twice-daily peaks in the diurnal precipitation cycle occur widely over the southern slopes of the Nepal Himalayas. The minimum rainfall rate that the TRMM PR sensor can detect is ~0.7 mm h^{-1}, which is higher than the rate for many precipitation events recorded at the AWS (Figure 2). The width of Rolwaling Valley is ~5 km around the AWS location, which is equivalent to the footprint for the TRMM PR sensor. Many valleys become narrower in high-elevation areas of the Himalayas than in lower elevation areas. The surface clutter in the PR observations from the complex deep valley system affects the precipitation measurements for high-elevation areas (Hirose et al., 2017b). These factors may limit the precipitation detection over higher elevations (>4,000 m) for the TRMM PR product.

Hereafter, we consider the areas of the Nepal Himalayas below and above ~1,500 m asl as lower and higher elevations, respectively. The lower elevations include the Sub-Himalayas (500–1,000 m), and the higher elevations include the Lesser and Greater Himalayas. Figure 6 shows that the higher elevations contain clusters 5 and 7 (each with two precipitation peaks), and the lower elevations contain clusters 4 and 6 (each with a single precipitation peak).

3.1.3. Precipitation Properties of the Two Precipitation Maxima

Precipitation properties can provide information that is useful for understanding the mechanisms that drive a precipitation system. Figure 7 shows how the properties of precipitation in the TRMM PR data vary with latitude and time-of-day around Rolwaling Valley. Precipitation occurs to the south of 27.2°N, where the surface elevation is less than 500 m asl, until 10:00 LT. After 12:00 LT, precipitation occurs widely over slopes that are between 500 and 4,000 m asl (from 27° to 28°N), with maxima at around 27.3° and 27.6°N (Figure 7a). Precipitation seems to start earlier in the day at lower elevations than at higher elevations. At the peak around 2,000 m asl, precipitation decreases at around 18:00 LT, increases again afterward, and has a maximum at around 23:00–00:00 LT. This clear nighttime precipitation enhancement at around 2,000 m asl extends from 27.5°N to 28.0°N. The precipitation continues until 03:00 LT, after which the area of high precipitation shifts rapidly south of 27.2°N. The diurnal pattern of precipitation is similar to that for precipitation frequency (Figure 7b). The conditional rain rate is higher over lower than higher-elevation areas, and tends to be higher in the nighttime than daytime (Figure 7c). One striking feature in Figure 7 is that the area where convective rain accounts for a high proportion of the precipitation (>50%) spreads from lower-to-higher-elevation terrain during the day, and stratiform rain increases at night over higher-elevation terrain (Figures 7d and 7e). The height of the precipitation system is less than 6,500 m asl during the day, whereas it exceeds 7,000 m asl at night (Figure 7f). These results support our interpretation of the spatial and temporal differences between precipitation patterns in the TRMM PR and IMERG products (Figure 5).

We can determine which features are common to the diurnal precipitation cycle throughout the Nepal Himalayas, and which patterns are region-specific, by looking at how precipitation varies with latitude and time-of-day in different 1° longitude bands (Figure 8). Features common to the diurnal precipitation cycle throughout the Nepal Himalayas are the double peaks in precipitation rate that occur in two zones of rapidly increasing relief and at steps in the topographic profile between 500 and 1,000 m asl, and at around

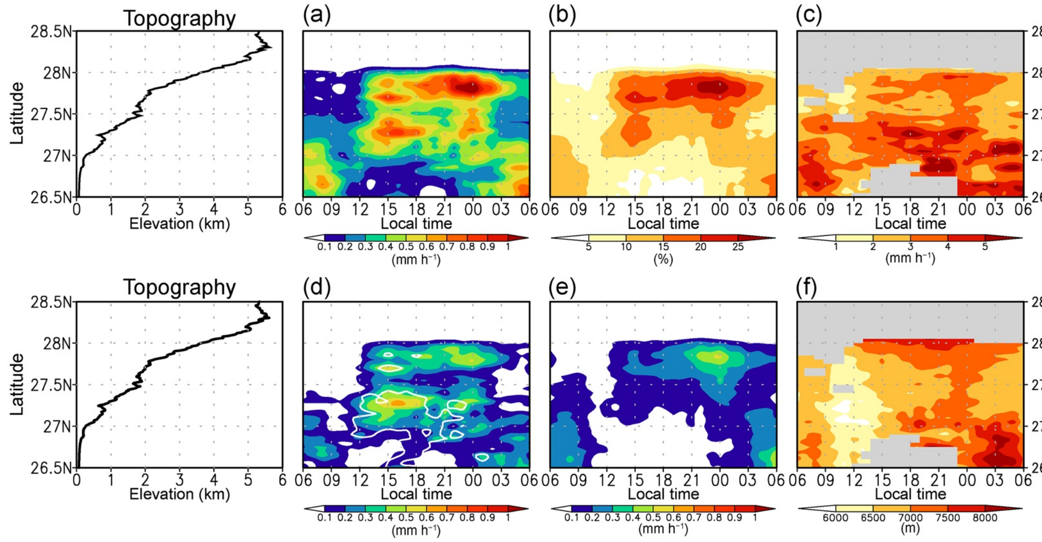

Figure 7. Left panels: average surface elevation between 86.5° and 87.5°E from GMTED2010 data (km asl). Latitude-time (local time at 90°E) cross-sections of precipitation properties from the Tropical Rainfall Measuring Mission (TRMM) precipitation radar (PR) data between 86.5° and 87.5°E in summer (June–September) for 17 years (1998–2014): (a) unconditional rain rate (mm h^{-1}); (b) precipitation frequency (%); (c) conditional rain rate (mm h^{-1}); (d) convective-type rainfall (shading; mm h^{-1}), white contours show where convective-type rain accounts for 50% of the total rainfall; (e) stratiform-type rainfall (mm h^{-1}); and (f) storm height above sea level (shading, m). Grid cells where the precipitation frequency is less than 5% are omitted and shaded in gray in (c) and (f). The plotted data show the 3-h running mean for all fields.

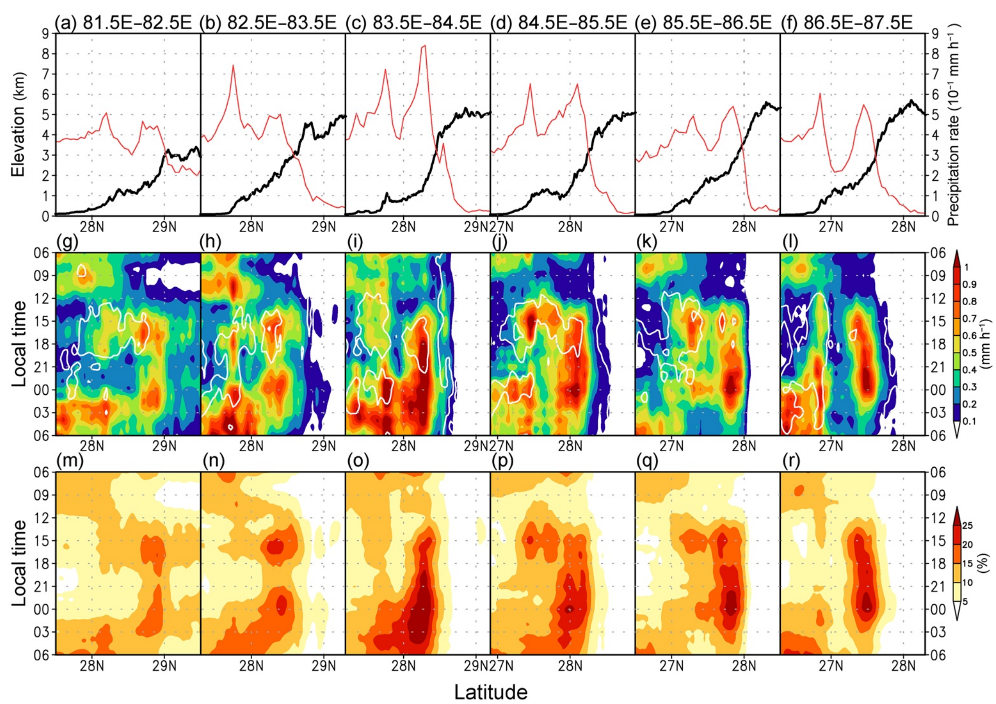

Figure 8. Variations in precipitation properties with latitude and time-of-day, in 1° longitude bands from 81.5°−82.5°E to 86.5°−87.5°E, in the Nepal Himalayas. Panels in the same vertical column show data from the same longitude band. Top panels (a–f): average elevation (km; thick solid line) from GMTED2010, and precipitation amount ($\times 10^{-1}$ mm h^{-1}; thin red solid line). Middle panels (g–l): latitude-time cross-sections of unconditional rain rate (mm h^{-1}; shading), white contours show where convective-type rain accounts for 50% of the total precipitation. Bottom panels (m–r): As in (g–l) but for precipitation frequency (%). Data plotted in (g–r) are the 3-h running means.

2,000 m asl (Figures 8a–8f), which is similar to the results of Bookhagen and Burbank (2006). The diurnal patterns of precipitation rate (Figures 8g–8l) are similar to those of rain frequency (Figures 8m–8r) for all longitudes, which indicates that the precipitation amount is determined primarily by rainfall frequency. The proportion of precipitation that is accounted for by convective-type rain is higher in the daytime at higher elevations but decreases during the night, meaning that stratiform-type precipitation is enhanced over terrain at higher elevations (Figures 8g–8l). This suggests that different mechanisms may be responsible for the daytime and nighttime peaks in precipitation. The difference over the longitude bands shows that precipitation rate and frequency over the central Nepal Himalayas, between 83.5° and 85.5°E, are highest over higher elevations (Figures 8c and 8d).

3.2. Diurnal Cycle of Atmospheric Circulation

The in situ observation and TRMM PR data show that twice-daily maxima occur for precipitation throughout the Nepal Himalayas, including over the high-elevation glacierized area, as described above. The twice-daily maxima observed at AWSs that are located higher than 4,000 m asl (in our study and others) are likely generated by the same mechanism as the maxima in the TRMM PR data. The bimodal shape of the diurnal cycle for different precipitation properties suggests that there is a common driving force for the two maxima across the Nepal Himalayas.

The topography in the ERA5 data set captures slope angles and elevations well, except regional-scale topographies (Figure 9). Southeasterly moisture fluxes directed toward the southern slopes of the Himalayas can be seen throughout the day at longitudes around Rolwaling Valley (Figures 9a and 9b). The moisture flux strengthens twice a day, once during the day and once at night, creating maxima in the southerly component of the flux at 12:00 and 00:00 LT, and a minimum at around 17:00 LT from the foothills to the southern slopes of the Himalayas (Figure 9a). The timing of the strengthening of the moisture inflow toward the southern slopes corresponds closely to the twice-daily maxima observed at the AWS in Rolwaling Valley (Figure 3) and in the TRMM PR data (Figure 6i). The area over which the southerlies are enhanced extends from the foothills to higher-elevation areas of the Himalayas during the day, and extends up to the Gangetic Plain at night. The easterly component of the moisture flux also has two maxima, at 09:00 and 00:00 LT (Figure 9b). A local maximum occurs in the easterly moisture flux over the foothills of the Himalayas. The twice-daily strengthening of the moisture flux that flows toward the Himalayas drives moisture flux convergence over the southern slopes twice a day (Figure 9c), providing conditions favorable for condensation over the slopes. The same features can be found at other longitudes in the Nepal Himalayas (figures not shown).

To determine which pressure levels control the diurnal variations in the vertically integrated moisture flux in Figure 9, the vertical distribution of the wind fields over the windward plain immediately in front of the Himalayas is plotted against time-of-day in Figures 10a and 10b. Both the meridional and zonal wind components fluctuate diurnally in the lower atmosphere below 800 hPa. The diurnal variations in wind speed and direction reflect the development of the atmospheric boundary layer. From 10:00 to 18:00 LT, the vertical gradient for potential temperature becomes small below 900 hPa, because of active dry convection that is driven by daytime surface heating (Figure 10c). Simultaneously, the surfaces of the southern slopes in the Himalayas are heated by solar radiation and the heated slope surfaces induce upslope flows. This causes the northward component of the wind to accelerate over the plain in front of the Himalayas, leading to the maximum meridional wind speed at around 14:00 LT (Figure 10a). Both the meridional and zonal components of the wind are at a minimum between 16:00 and 17:00 LT. After 18:00 LT, surface cooling after sunset generates a stable surface layer during the night (Figures 10a–10c). Then, both components of the wind accelerate to reach their maximum speed at around 00:00 LT at 925 hPa (~700 m asl). After 03:00 LT, when precipitation weakens over the terrain above 500 m asl and enhances below 500 m asl (Figures 7 and 8), the meridional component of the wind, which flows toward the southern slopes, becomes weaker relative to its strength at the two peak times, but the easterly winds remain strong (Figure 10b).

In the downslope side of the maximum rainfall at ~2,000 m asl over the slopes, the southerly component of the horizontal moisture flux also has two maxima, at around 12:00 and 23:00 LT (Figure 10d). The value for the daytime peak is larger than that of the nighttime peak, which reflects a gentle upslope flow at nighttime. The maximum wind speed at the daytime peak appears close to the surface, whereas the nighttime peak occurs higher up. The different vertical position of the meridional wind maximum at night may explain the

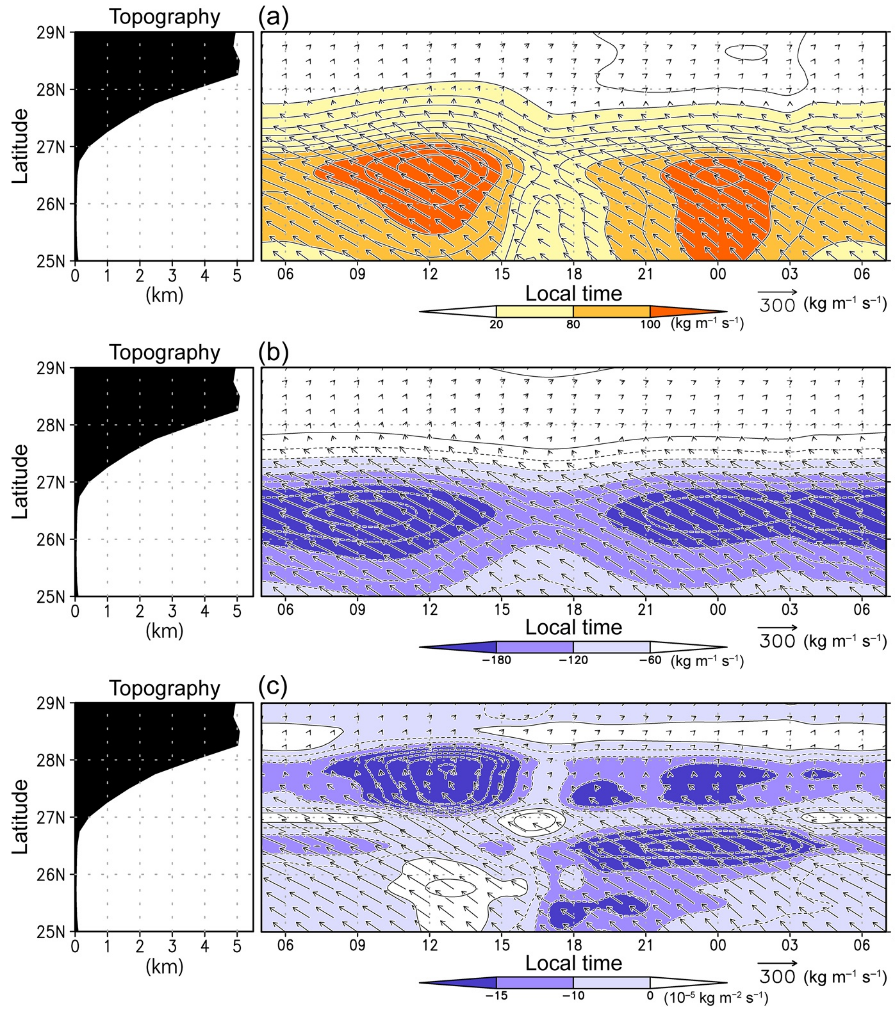

Figure 9. (a) Latitude-time (local time at 90°E) cross-sections of vertically integrated water-vapor flux (vectors; kg m^{-1} s^{-1}) and the meridional component of water-vapor flux (shading; kg m^{-1} s^{-1}) averaged over 85.5°–86.5°E. (b) and (c) As in (a) but for the zonal component of water-vapor flux (shading; kg m^{-1} s^{-1}) and divergence of water-vapor flux (shading; $\times 10^{-5}$ kg m^{-2} s^{-1}), respectively. Panels to the left of each plot show the average elevation for 85.5–86.5°E (km asl) from ERA5 data. The composite diurnal cycle was constructed by averaging ERA5 reanalysis data for each hour during summer (June–September) for 17 years (1998–2014).

nighttime precipitation maximum under weak surface wind conditions at the Rolwaling AWS (Figure 4). Daytime surface heating causes greater instability in the near-surface atmosphere (Figures 10d and 10e), which suggests that convective-type rainfall dominate precipitation during the day. In contrast, the degree of instability reduces at night due to the decrease in surface heating, and the near-surface atmosphere is nearly neutral, or weakly stable in moist convections.

The meridional wind circulation and convergence of horizontal moisture fluxes at different pressure levels is shown in Figure 11. During the day, upslope flows are evident near slopes from lower to higher elevations in the Himalayas. Moisture flux convergence occurs within a thin atmospheric layer along the surface of the slopes (Figures 11a–11f). At night, the near-surface upslope flows weaken, and the southerly airflow toward the Himalayas is enhanced at 950–900 hPa (500–700 m asl) over the foothills. Large-scale moisture flux convergence occurs over terrain stretching from the foothills to higher elevations in the Himalayas, and is associated with the intrusion of stronger low-level monsoon flows (Figures 11g–11l). A local maximum for moisture flux convergence occurs at around ~800 hPa (~2,000 m asl) on slopes at every longitude, corresponding to the band of high nighttime precipitation (Figures 5c, 5f and 8). The strengthening of moisture flux convergence results in a bimodal temporal distribution of upward motion over the southern slopes of

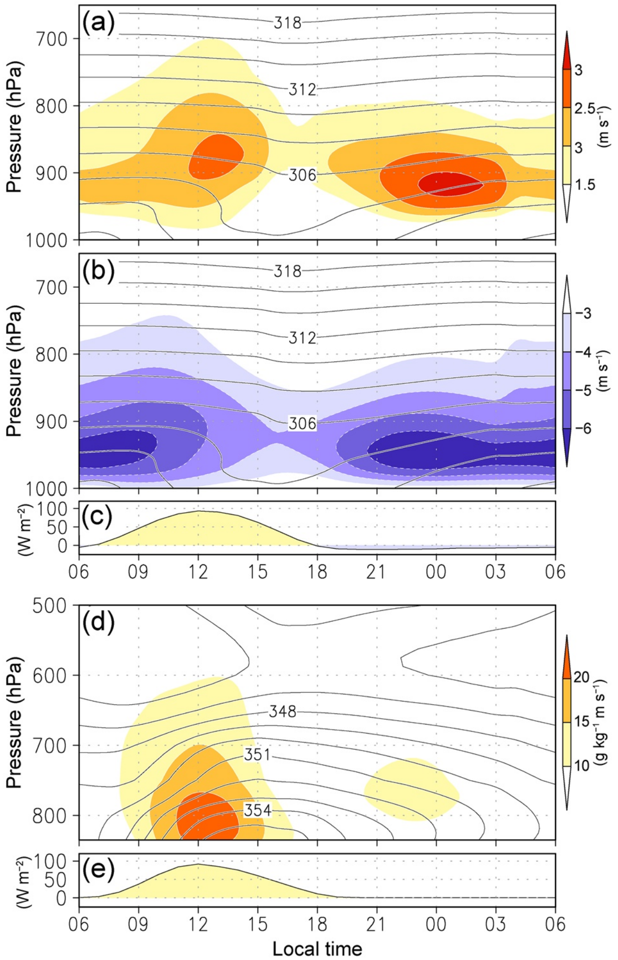

Figure 10. (a) Height-time cross-section of meridional wind (shading; m s^{-1}) and potential temperature (contours at 2 K intervals) over the plain in front of the Himalayan slopes at 26.5°N, averaged over 85.5°–86.5°E. (b) As in (a) but for zonal wind (shading; m s^{-1}) and potential temperature (contours at 2 K intervals). (c) Time series of surface sensible heat flux (W m^{-2}) over the plain, averaged over 25.5°–26.5°N and 85.5°–86.5°E. (d) Height-time cross-section of meridional component of the horizontal moisture flux (shading; g kg^{-1} m s^{-1}) and equivalent potential temperature (contours at 1 K intervals) over the slopes at 27.5°N, averaged over 85.5°–86.5°E. Note that the latitude in (d) is different from that in (a) and (b). (e) As in (c) but for 27.5°N, averaged over 85.5°–86.5°E.

the Himalayas (Figures 11m–11r). Heaviest precipitation occurs in the central Nepal Himalayas (Figure 8c) with strong upward motion (Figure 11o) because the large southeasterly moisture flux meets terrain with southern-southeastern-facing slopes (Figure 1a).

Large-scale moisture flux anomalies are related to the double diurnal peaks of precipitation, and highlight the different spatial scales that create the twice-daily maxima (Figure 12). In the daily mean fields, a monsoon trough over the Indian subcontinent drives southeasterly moisture fluxes toward the Nepal Himalayas (Figure 12a). Moist onshore winds from the Bay of Bengal can intrude toward the Nepal Himalayas over the Gangetic Plain. At the daytime peak of precipitation, northward moisture flux anomalies occur only over and around the Himalayas, reflecting the daytime upslope flows over the southern slopes (Figure 12b). The break period between the two peaks is characterized by large northwesterly moisture flux anomalies over the southern slopes and the Gangetic Plain, which represent the deceleration of upslope flows over the southern slopes and onshore monsoon flows over the Gangetic Plain (Figure 12c). At the time of the nighttime peak, strong southwesterly moisture flux anomalies appear along the eastern coast of the Indian subcontinent (Figure 12d). The southwesterly moisture flux anomalies encounter the Meghalaya Plateau and become a major source for nocturnal precipitation over the southern slopes of the plateau (Fujinami et al., 2017). Part of the anomalous southwesterly moisture flux turns northwestward toward the southern slopes of the Nepal Himalayas. The southerly anomalies reach the foothills of the Himalayas, and the weak northerly anomalies appear over the southern slopes. The anomaly fields mean that the onshore south-southeasterly monsoon flow of moist air from the Bay of Bengal toward the Himalayas is enhanced up to the foothills of the Himalayas relative to the daily mean total fields, with southeasterly moisture flow weakening slightly over the southern slopes (Figure 9). This situation is favorable for inducing large-scale moisture flux convergence over the southern slopes during nighttime, as shown in Figures 11g–11l.

4. Discussion

4.1. Generation Mechanisms for Twice-Daily Precipitation Maxima

This study suggests that the twice-daily precipitation maxima are typical features of the diurnal cycle of precipitation over the Nepal Himalayas, particularly for high-elevation areas, which includes the glacierized area. Upslope flows over the mountainsides during the day, and acceleration of the low-level monsoon flow to the south of the Himalayas at night, may be the major drivers of the twice-daily precipitation maxima. Land surface effects such as surface heating and cooling regulate low-level wind speed and wind direction above the ground through the atmospheric boundary layer over both the Himalayan slopes and the Gangetic Plain to the south.

During daytime, upslope flows occur across entire slopes from the foothills to high-elevation areas due to daytime heating of slope surfaces (Figures 4b, 4c, Figures 10d and 10e). The double bands of rainfall occur along strikes between ~500 and 1,000 m asl, and at ~2,000 m asl (Figures 5–8). These altitudes correspond to areas where slope gradients become drastically steep and comprise the "steps" for the two-step orography of the Nepal Himalayas (Figure 8). The upslope flows frequently decelerate (i.e., converge) at around 500–1,000 m asl and at ~2,000 m asl, resulting in two clear rainbands with a dominance of convective-type precipitation during daytime (Figures 7 and 8). Valleys and ridges at regional scales of <10 km can modulate the phase and amplitude of the daytime precipitation peak. Further detailed investigation is required

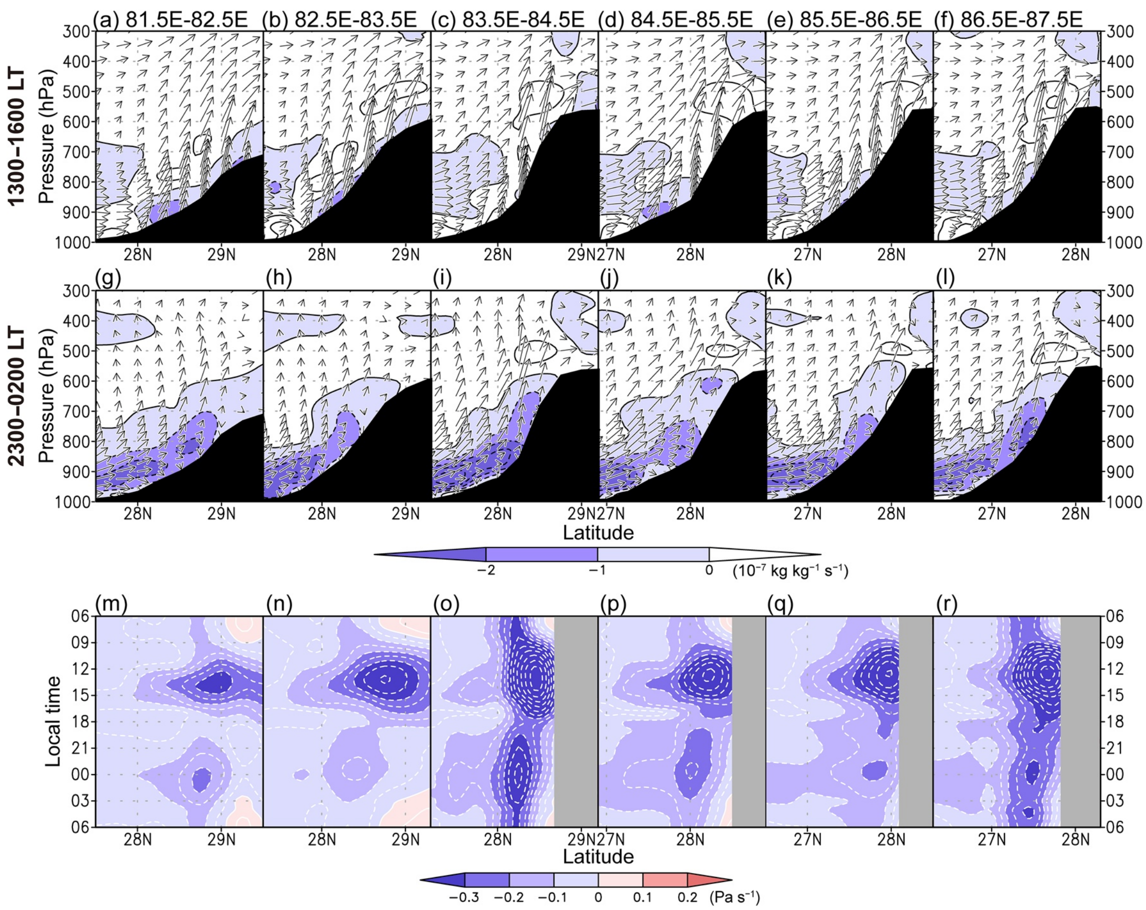

Figure 11. (a–f) Latitude-height cross-sections of meridional and vertical winds (vectors; vertical wind is multiplied by 10) and the horizontal water-vapor flux divergence (shading; $\times 10^{-7}$ kg kg^{-1} s^{-1}) for 13:00–16:00 LT (07:00–10:00 UTC), averaged over 1° longitude bands between 81.5° and 87.5°E in the Nepal Himalayas. LT is local time at 90°E. Black shading shows the topography from ERA5 data. (g–l) As in (a–f) but for 23:00–02:00 LT (17:00–20:00 UTC). (m–r) Latitude-time (local time) cross-sections of the vertical velocity (ω; Pa s^{-1}) at 600 hPa, averaged over 1° longitude bands between 81.5°E and 87.5°E. Panels in the same vertical column show data from the same longitude band.

to elucidate the regional difference in the diurnal cycle. In contrast, over the plain, the vertically well-mixed layer (due to surface heating) decelerates the low-level horizontal wind speed toward the Himalayas because vertical mixing in the mixed or sub-cloud layers provides frictional drag on the horizontal wind (Figures 9 and 10).

After sunset over the slopes, upslope winds that promote condensation near the surface during daytime are weakest at 20:00 LT (Figures 4c and 10d), resulting in a break in precipitation. In contrast, over the plain to the south of the Himalayas, low-level winds toward the Himalayas start to accelerate at 950–900 hPa (500–950 m asl) and are strongest at 00:00 LT (Figure 10). This nocturnal wind acceleration can be interpreted as a nocturnal jet over the Gangetic Plain, driven by the decreased surface friction over the stable nocturnal boundary layer due to surface cooling (Blackadar, 1957; Fujinami et al., 2017; Terao et al., 2006; Van de Wiel et al., 2010). Thus, moist low-level monsoon flows from the Gangetic Plain reach the Himalayas at night, causing large-scale moisture flux convergence around the southern slopes. As the flows move toward the high-elevation Himalayas, they become subject to gentle orographic lift, which enhances stratiform-type rainfall. The rainfall peak is clearer at higher elevations (~2,000 m asl) than at lower elevations (500–1,000 m asl). A single nighttime peak of precipitation occurs over areas at elevations below ~1,500 m asl, with the exception of areas between ~500 and 1,000 m asl. This means that nighttime precipitation occurs widely over the slopes from plain in front of the Himalayas to higher-elevation areas. The moist monsoon flows have a jet-like vertical structure; at night, these may pass over the first range of the Himalayas (i.e., Sub-Himalayas), which is at ~500 m asl,

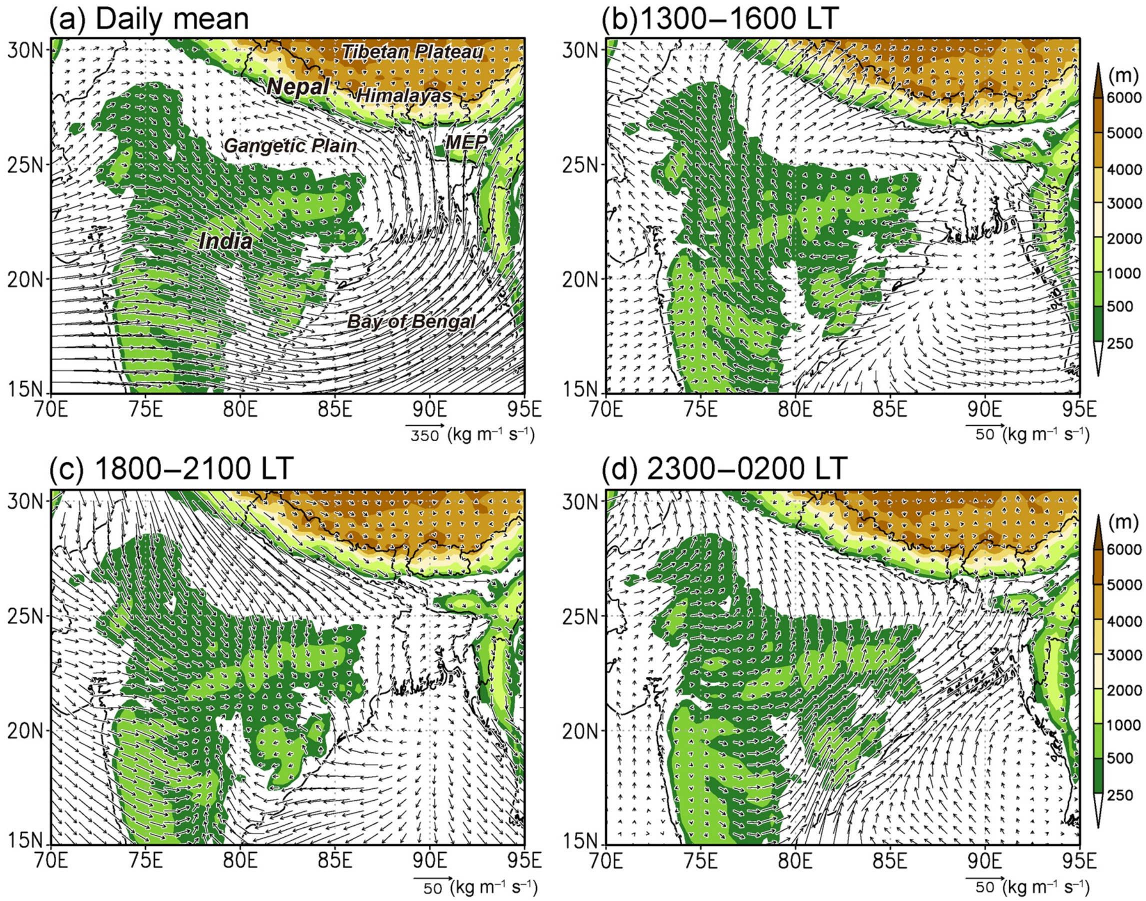

Figure 12. (a) Daily mean vertically integrated water-vapor flux (vectors; kg m^{-1} s^{-1}) in summer (June–September) for 1998–2014 (17 years). Shading represents topography from ERA5 reanalysis. Locations of terrains in the Himalayas, the Tibetan Plateau, the Meghalaya Plateau (MEP), and the Gangetic Plain are also shown. (b) Composite anomalies in vertically integrated water-vapor flux (vectors) between the mean value in 13:00–16:00 LT (07:00–10:00 UTC) and the daily mean. (c and d) As in (b), but for 18:00–21:00 LT (12:00–15:00 UTC) and 23:00–02:00 LT (17:00–20:00 UTC), respectively. LT is local time at 90°E.

without strongly impinging on the terrain, resulting in less precipitation there than at higher elevations (Figure 7). After 02:00 LT, the decrease in the southerly moisture flux suppresses the orographic lift of the flow at higher elevations (Figure 10a). Meanwhile, the easterly moisture flux remains strong, possibly allowing it to interact more easily with low-level monsoon flows around the Sub-Himalayas, which may drive the southward shift of high precipitation areas in the foothills of the Himalayas (<~500 m asl; Figures 7 and 8).

The enhancement and southward movement of nocturnal rainfall might result from downslope flows (gravity currents) caused by radiative cooling on the slope surface and downdraft owing to evaporative cooling and precipitation drag from moist convection over the slopes, alongside the interactions of these factors with preexisting southerly monsoon flows from the plain (e.g., Bhatt & Nakamura, 2006). However, there is no evidence of nighttime downslope flows in the summer AWS observations (Figure 4), whereas upslope flows can be clearly seen in daytime. This asymmetry is consistent with results from in situ observations in other studies (Barros & Lang, 2003; Shea et al., 2015; Ueno et al., 2001, 2008). The downslope flows may be agents for local precipitation enhancement, but these results suggest that it is not the primary diver for the nighttime peak in precipitation at higher elevations. Cloud-top radiative cooling may enhance nighttime precipitation (Bhatt & Nakamura, 2006), since tall and wide precipitation systems and cloud-systems develop at night over terrain at higher elevations (Figures 5c and 5f). Cloud-resolving numerical model simulations with a high spatial resolution of at least 1–2 km may help to explain these detailed precipitation processes, and may also provide insights for the nighttime precipitation. Investigation of a diurnal cycle in the vertical wind structure over the plains and higher-elevation areas by in situ observations is necessary to confirm that the proposed mechanisms explain the twice-daily precipitation maxima in the ERA5.

4.2. Precipitation Over Higher-Elevation Terrain Near the Glacier

Our study shows that twice-daily maxima occur over the glacierized high-elevation area (Figure 3). The diurnal cycle is controlled by atmospheric circulation at scales large enough to encompass all Himalayan slopes and the South Asian monsoon. Local wind systems mean that valleys, such as the Rolwaling Valley (Figure 1b), can act as channels that transport moisture to higher elevations (Lin et al., 2018). During the day, upslope flows along the valley also promote condensation. Potter et al. (2018) showed that glaciers in the Himalayas cause upvalley flows to decelerate around the glacierized area, owing to the daytime reduction in pressure gradient, which is the gradient that drives the upvalley flows. Without the glacier, the upvalley wind would continue to higher elevations. The deceleration of upvalley flows can induce a local moisture convergence, which suggests that precipitation in the glacierized area is enhanced by the existence of glacier itself. Daytime precipitation at the Rolwaling AWS may be enhanced by such a glacier-valley wind system because the AWS is located at the terminal of Trakarding glacier, resulting in the distinct daytime precipitation maximum. In addition, in the downslope side of the AWS, Tsho Rolpa Lake, the largest glacial lake in Nepal, is located close to the AWS (Figure 1b in the present study and Figure 1 of Sunako et al., 2019). Evaporation from the lake surface may supply water vapor to upvalley flows during daytime as an elevated humidifier, enhancing precipitation around the Trakarding-Trambau glacier system. Himalayan glaciers are debris-covered (Fujita & Sakai, 2014), so their surfaces are darker-colored with lower albedo compared with bright debris-free glaciers (not considered by Potter et al., 2018). This means the Himalayan glaciers supply sensible heat flux to the atmosphere (e.g., Nicholson & Stiperski, 2020; Steiner et al. 2018), promoting water-vapor transport to higher elevations, up to the upper parts of the glaciers. Study of such systems will improve the understanding of the persistence mechanisms of Himalayan glaciers that are strongly affected by the South Asian monsoon.

Nocturnal precipitation is primarily induced by the gentle orographic uplift of moist monsoon flow from the south. The precipitation systems probably rise gradually as they travel along the valleys. Radiative cooling at higher elevations at night can also induce in situ condensation under weak surface wind conditions. Figure 4b shows that the rate of decrease for surface temperature became gradual after sunset at ~19:00 LT. This may be due in part to the release of latent heat from near-surface condensation processes. Understanding the vertical structure of the precipitation system, from the bottom of the valley to higher elevations, can provide insights into nocturnal precipitation.

Our results show that in situ observations are still important for capturing precipitation, and other meteorological data, over the high-elevation glacierized area of the Himalayas. However, a single rain gauge is unlikely to be spatially representative. To address this, observations from space-borne precipitation radar are necessary, although the TRMM PR product may fail to accurately detect precipitation at elevations of >4,000 m asl. Further climatology studies into diurnal precipitation cycles, and research into the vertical structure of precipitation in the Himalayas, are expected to be undertaken by using GPM DPR in the future. However, it might be difficult to observe vertical precipitation structure, even from GPM DPR, because of surface clutters created by the deep valley system. If precipitation systems traveling close to the valley bottoms are widespread in the high Himalayas, then space-borne radar observation systems will fail to detect precipitation accurately. Ground-based precipitation measurements and precipitation/cloud radar observations are also required so that the detailed vertical structure of precipitation throughout the day can be understood.

5. Summary

This study investigated the diurnal cycle of summer precipitation over the Nepal Himalayas, from the foothills to the high-elevation glacierized area, using AWS observations recorded close to the glacier between 2016 and 2018, and 17 years (1998–2014) of TRMM PR and 15 years (2000–2014) of IMERG data. The mechanisms that drive the observed diurnal cycle were investigated using ERA5.

We found twice-daily maxima in the diurnal precipitation cycle observed at an AWS, which was located at 4,806 m asl, close to Trakarding Glacier in Rolwaling Valley, eastern Nepal Himalayas. Precipitation increased twice daily, with a daytime peak between 14:00 and 16:00 LT, and a nighttime peak between 00:00 and 02:00 LT. The precipitation amounts were similar for the two peaks, with a break between the peaks at around 20:00 LT. A minimum in the diurnal precipitation cycle occurred at 10:00 LT. More than 80% of the total precipitation fell with a weak intensity of <1 mm h^{-1}, but had a high occurrence frequency of around 50%. The daytime peak in precipitation resulted from upslope flows along the valley that were driven by surface heating from incoming solar radiation, whereas the nighttime peak occurred when surface air flows were weak and almost saturated.

The TRMM PR and IMERG data sets have fine spatial and temporal resolution. TRMM PR showed a double band of rainfall over the southern slopes of the Himalayas when the daytime precipitation peak was observed at the AWS in Rolwaling Valley. The two rainfall bands were over terrain between 500 and 1,000 m asl, and at ~2,000 m asl. These altitudes correspond to two zones where the slope gradients steepen rapidly, creating steps in the topographic profile of the Himalayas. The rainfall band at higher elevations (>1,500 m asl) strengthened at the time the nighttime peak was recorded at the AWS. Cluster analysis of the diurnal cycles of precipitation frequency in the TRMM PR data showed that a diurnal precipitation cycle with two maxima occurred widely across the Nepal Himalayas. The twice-daily precipitation maxima that were observed at the AWS in Rolwaling Valley were probably driven by similar factors to those that drove the precipitation maxima seen at ~2,000 m asl. Precipitation in the daytime was mostly convective-type rain, with a lower rain-top height over terrain at both lower and higher elevations, whereas nighttime precipitation was more likely to be stratiform-type rain, with a higher rain-top height over higher-elevation terrain.

ERA5 shows diurnal cycles in atmospheric circulation that may offer reasonable explanations for the twice-daily precipitation maxima. Monsoon air flows into the Himalayas from the southeast in summer. The moisture fluxes toward the southern slopes of the Himalayas were enhanced twice a day, with a daytime peak at around 12:00 LT and a nighttime peak at around 00:00 LT. This suggests that the moisture fluxes were likely to converge twice a day over the slopes, resulting in the twice-daily precipitation maxima that were observed at the AWS in Rolwaling Valley, and which also occur in the TRMM PR data. The diurnal cycle of the vertically integrated moisture flux is controlled by horizontal winds in the atmospheric boundary layer.

Daytime surface heating, caused by incoming solar radiation, created upslope flows, which led to condensation over the slopes and a daytime peak in precipitation. The Gangetic Plain, which is windward of the Himalayas, also experienced surface heating. The development of the atmospheric mixed layer during the day reduced the horizontal wind speeds over the plain, because the vertical motion in the layer acted as a frictional drag. The moisture flux toward the Himalayas therefore weakened after 15:00 LT. After sunset (~19:00 LT), a stable nocturnal boundary layer formed over the surface over the plain, owing to the radiative cooling. The horizontal wind at 950–800 hPa (500–2,000 m asl) accelerated toward the Himalayas as the frictional drag from vertical mixing over the windward plain decreased. The nocturnal jet enhanced precipitation over the southern slopes of the Himalayas by promoting gentle orographic uplift of the moist onshore monsoon flows. To summarize, interactions between the land and atmosphere over the Himalayas and the Gangetic Plain create two maxima in the diurnal precipitation cycle over the Nepal Himalayas.

Day-to-day fluctuations (Figures 2b, 2d and 2f) are actually effects of synoptic-scale atmospheric circulation at midlatitudes and in the tropics in summer. The diurnal cycles of summer precipitation are modulated by synoptic-scale low-pressure systems, such as monsoon depressions (Fujinami et al., 2020) and mid-latitude troughs (Bohlinger et al., 2017, 2019), and by intraseasonal oscillations that occur in many places in the midlatitudes and tropics (Fujinami & Yasunari, 2004; Fujinami et al., 2011, 2014). Understanding how diurnal precipitation cycles are modulated by these patterns on multiple spatiotemporal scales is essential for full understanding of precipitation variability, and warrants further investigation.

Data Availability Statement

The in situ observation data in Rolwaling Valley are available from PANGEA (https://doi.pangaea.de/10.1594/PANGAEA.931159). The TRMM PR data and IMERG data used here were provided by Japan Aerospace Exploration Agency (JAXA) (https://www.gportal.jaxa.jp/gp/top.html). The ERA5 reanalysis data were downloaded from the Copernicus climate-change service (C3S) climate date store (https://cds.climate.copernicus.eu). GMTED2010 data are available from the US. Geological Survey (https://topotools.cr.usgs.gov/gmted_viewer/viewer.htm). ASTER GDEM3 data are available from the NASA EARTHDATA (https://earthdata.nasa.gov/).

Acknowledgments

The authors thank H. Masunaga and M. Hirose for helpful discussions. This study was conducted with support from JSPS KAKENHI grant Nos. 18KK0098, 19H01375, and 20H02252, and from JSPS and SNSF under the Joint Research Projects (JRPs: 20191503) scheme. Portions of this study were conducted as part of a collaborative research program of the Institute for Space-Earth Environmental Research, Nagoya University.

References

Barros, A. P., Joshi, M., Putkonen, J., & Burbank, D. W. (2000). A study of the 1999 monsoon rainfall in a mountainous region in central Nepal using TRMM products and rain gauge observations. *Geophysical Research Letters*, *27*, 3683–3686. https://doi.org/10.1029/2000GL011827

Barros, A. P., Kim, G., Williams, E., & Nesbitt, S. W. (2004). Probing orographic controls in the Himalayas during the monsoon using satellite imagery. *Natural Hazards and Earth System Sciences*, *4*, 29–51. https://doi.org/10.5194/nhess-4-29-2004

Barros, A. P., & Lang, T. J. (2003). Monitoring the monsoon in the Himalayas: Observations in central Nepal, June 2001. *Monthly Weather Review*, *131*, 1408–1427. https://doi.org/10.1175/1520-0493(2003)131<1408:MTMITH>2.0.CO;2

Bhatt, B. C., & Nakamura, K. (2005). Characteristics of monsoon rainfall around the Himalayas revealed by TRMM precipitation radar. *Monthly Weather Review*, *133*, 149–165. https://doi.org/10.1175/MWR-2846.1

Bhatt, B. C., & Nakamura, K. (2006). A climatological-dynamical analysis associated with precipitation around the southern part of the Himalayas. *Journal of Geophysical Research*, *111*, D02115. https://doi.org/10.1029/2005JD006197

Biasutti, M., Yuter, S. E., Burleyson, C. D., & Sobel, A. H. (2012). Very high resolution rainfall patterns measured by TRMM precipitation radar: Seasonal and diurnal cycles. *Climate Dynamics*, *39*, 239–258. https://doi.org/10.1007/s00382-011-1146-6

Blackadar, A. K. (1957). Boundary layer wind maxima and their significance for the growth of nocturnal inversions. *Bulletin of the American Meteorological Society*, *38*, 283–290. https://doi.org/10.1175/1520-0477-38.5.283

Bohlinger, P., Sorteberg, A., Liu, C. H., Rasmussen, R., Sodemann, H., & Ogawa, F. (2019). Multiscale characteristics of an extreme precipitation event over Nepal. *Quarterly Journal of the Royal Meteorological Society*, *145*, 179–196. https://doi.org/10.1002/qj.3418

Bohlinger, P., Sorteberg, A., & Sodemann, H. (2017). Synoptic conditions and moisture sources actuating extreme precipitation in Nepal. *Journal of Geophysical Research: Atmospheres*, *122*, 12653–12671. https://doi.org/10.1002/2017JD027543

Bolton, D. (1980). The computation of equivalent potential temperature. *Monthly Weather Review*, *108*, 1046–1053. https://doi.org/10.1175/1520-0493(1980)108<1046:TCOEPT>2.0.CO;2

Bookhagen, B. (2010). Appearance of extreme monsoonal rainfall events and their impact on erosion in the Himalaya. *Geomatics, Natural Hazards and Risk*, *1*, 37–50. https://doi.org/10.1080/19475701003625737

Bookhagen, B., & Burbank, D. W. (2006). Topography, relief, and TRMM-derived rainfall variations along the Himalaya. *Geophysical Research Letters*, *33*, L08405. https://doi.org/10.1029/2006GL026037

Boos, W. R., & Kuang, Z. M. (2010). Dominant control of the South Asian monsoon by orographic insulation versus plateau heating. *Nature*, *463*, 218–222. https://doi.org/10.1038/nature08707

Chen, G. (2020). Diurnal cycle of the Asian summer monsoon: Air pump of the second kind. *Journal of Climate*, *33*, 1747–1775. https://doi.org/10.1175/JCLI-D-19-0210.1

Fu, Y., Pan, X., Xian, T., Liu, G., Zhong, L., Liu, Q., et al. (2018), Precipitation characteristics over the steep slope of the Himalayas in rainy season observed by TRMM PR and VIRS. *Climate Dynamics*, *51*, 1971–1989. https://doi.org/10.1007/s00382-017-3992-3

Fujinami, H., Hatsuzuka, D., Yasunari, T., Hayashi, T., Terao, T., Murata, F., et al. (2011). Characteristic intraseasonal oscillation of rainfall and its effect on interannual variability over Bangladesh during boreal summer. *International Journal of Climatology*, *31*, 1192–1204. https://doi.org/10.1002/joc.2146

Fujinami, H., Hirata, H., Kato, M., & Tsuboki, K. (2020). Mesoscale precipitation systems and their role in the rapid development of a monsoon depression over the Bay of Bengal. *Quarterly Journal of the Royal Meteorological Society*, *146*, 267–283. https://doi.org/10.1002/qj.3672

Fujinami, H., Nomura, S., & Yasunari, T. (2005). Characteristics of diurnal variations in convection and precipitation over the southern Tibetan Plateau during summer. *SOLA*, *1*, 49–52. https://doi.org/10.2151/sola.2005-014

Fujinami, H., Sato, T., Kanamori, H., & Murata, F. (2017). Contrasting features of monsoon precipitation around the Meghalaya Plateau under westerly and easterly regimes. *Journal of Geophysical Research: Atmospheres*, *122*, 9591–9610. https://doi.org/10.1002/2016JD026116

Fujinami, H., & Yasunari, T. (2004). Submonthly variability of convection and circulation over and around the Tibetan Plateau during the boreal summer. *Journal of the Meteorological Society of Japan*, *82*, 1545–1564. https://doi.org/10.2151/jmsj.82.1545

Fujinami, H., Yasunari, T., & Morimoto, A. (2014). Dynamics of distinct intraseasonal oscillation in summer monsoon rainfall over the Meghalaya-Bangladesh-western Myanmar region: Covariability between the tropics and mid-latitudes. *Climate Dynamics*, *43*, 2147–2166. https://doi.org/10.1007/s00382-013-2040-1

Fujita, K., & Sakai, A. (2014). Modelling runoff from a Himalayan debris-covered glacier. *Hydrology Earth System Science*, *18*, 2679–2694. https://doi.org/10.5194/hess-18-2679-2014

Fujita, K., Sunako, S., & Sakai, A. (2021). *Meteorological observations at Trakarding glacier automatic weather station*. Rolwaling, Nepal: PANGAEA. Retrieved from https://doi.pangaea.de/10.1594/PANGAEA.931159

Hersbach, H., Bell, B., Berrisford, P., Hirahara, S., Horányi, A., Muñoz-Sabater, J., et al. (2020). The ERA5 global reanalysis. *Quarterly Journal of the Royal Meteorological Society*, *146*, 1999–2049. https://doi.org/10.1002/qj.3803

Hirose, M., Oki, R., Shimizu, S., Kachi, M., & Higashiuwatoko, T. (2008). Finescale diurnal rainfall statistics refined from eight years of TRMM PR data. *Journal of Applied Meteorology and Climatology*, *47*, 544–561. https://doi.org/10.1175/2007JAMC1559.1

Hirose, M., Takayabu, Y. N., Hamada, A., Shige, S., & Yamamoto, M. K. (2017a). Impact of long-term observation on the sampling characteristics of TRMM PR Precipitation. *Journal of Applied Meteorology and Climatology*, *56*, 713–723. https://doi.org/10.1175/JAMC-D-16-0115.1

Hirose, M., Takayabu, Y. N., Hamada, A., Shige, S., & Yamamoto, M. K. (2017b). Spatial contrast of geographically induced rainfall observed by TRMM PR. *Journal of Climate*, *30*, 4165–4184. https://doi.org/10.1175/JCLI-D-16-0442.1

Houze, R. A., Wilton, D. C., & Smull, B. F. (2007). Monsoon convection in the Himalayan region as seen by the TRMM Precipitation Radar. *Quarterly Journal of the Royal Meteorological Society*, *133*, 1389–1411. https://doi.org/10.1002/qj.106

Huffman, G. J., Bolvin, D. T., Braithwaite, D., Hsu, K., Joyce, R., Kidd, C., et al. (2019). *NASA Global Precipitation Measurement (GPM) integrated multi-satellite retrievals for GPM (IMERG). Algorithm theoretical basis document version 06, 38*. Retrieved from https://gpm.nasa.gov/sites/default/files/2019-05/IMERG_ATBD_V06.pdf

Huffman, G. J., Bolvin, D. T., Nelkin, E. J., Stocker, E. F., & Tan, J. (2020). *V06 IMERG release notes*. Retrieved from https://docserver.gesdisc.eosdis.nasa.gov/public/project/GPM/IMERG_V06_release_notes.pdf

Iguchi, T., Kozu, T., Meneghini, R., Awaka, J., & Okamoto, K. (2000). Rain-profiling algorithm for the TRMM precipitation radar. *Journal of Applied Meteorology*, *39*, 2038–2052. https://doi.org/10.1175/1520-0450(2001)040<2038:RPAFTT>2.0.CO;2

Immerzeel, W. W., van Beek, L. P. H., & Bierkens, M. F. P. (2010). Climate change will affect the Asian water towers. *Science*, *328*, 1382–1385. https://doi.org/10.1126/science.1183188

Kummerow, C., Barnes, W., Kozu, T., Shiue, J., & Simpson, J. (1998). The Tropical Rainfall Measuring Mission (TRMM) sensor package. *Journal of Atmospheric and Oceanic Technology*, *15*, 809–817. https://doi.org/10.1175/1520-0426(1998)015<0809:TTRMMT>2.0.CO;2

Kurosaki, Y., & Kimura, F. (2002). Relationship between topography and daytime cloud activity around Tibetan Plateau. *Journal of the Meteorological Society of Japan*, *80*, 1339–1355. https://doi.org/10.2151/jmsj.80.1339

Lin, C., Chen, D., Yang, K., & Ou, T. (2018). Impact of model resolution on simulating the water vapor transport through the central Himalayas: Implication for models' wet bias over the Tibetan Plateau. *Climate Dynamics*, *51*, 3195–3207. https://doi.org/10.1007/s00382-018-4074-x

Martens, B., Schumacher, D. L., Wouters, H., Muñoz-Sabater, J., Verhoest, N. E. C., & Miralles, D. G. (2020). Evaluating the land-surface energy partitioning in ERA5. *Geoscientific Model Development*, *13*(9), 4159–4181. https://doi.org/10.5194/gmd-13-4159-2020

Marzeion, B., Hock, R., Anderson, B., Bliss, A., Champollion, N., Fujita, K., et al. (2020). Partitioning the uncertainty of ensemble projections of global glacier mass change. *Earth's Future*, *8*, e2019EF001470. https://doi.org/10.1029/2019EF001470

Medina, S., Houze, R. A., Kumar, A., & Niyogi, D. (2010). Summer monsoon convection in the Himalayan region: Terrain and land cover effects. *Quarterly Journal of the Royal Meteorological Society*, *136*, 593–616. https://doi.org/10.1002/qj.601

Nicholson, L., & Stiperski, I. (2020). Comparison of turbulent structures and energy fluxes over exposed and debris-covered glacier ice. *Journal of Glaciology*, *66*, 543–555. https://doi.org/10.1017/jog.2020.23

Ohsawa, T., Ueda, H., Hayashi, T., Watanabe, A., & Matsumoto, J. (2001). Diurnal variations of convective activity and rainfall in tropical Asia. *Journal of the Meteorological Society of Japan*, *79*, 333–352. https://doi.org/10.2151/jmsj.79.333

Ouyang, L., Yang, K., Lu, H., Chen, Y., Zhou, X., & Wang, Y. (2020). Ground-based observations reveal unique valley precipitation patterns in the Central Himalaya. *Journal of Geophysical Research: Atmospheres*, *125*, e2019JD031502. https://doi.org/10.1029/2019JD031502

Potter, E. R., Orr, A., Willis, I. C., Bannister, D., & Salerno, F. (2018). Dynamical drivers of the local wind regime in a Himalayan Valley. *Journal of Geophysical Research: Atmospheres*, *123*, 13–186. https://doi.org/10.1029/2018JD029427

Sakai, A., & Fujita, K. (2017). Contrasting glacier responses to recent climate change in high-mountain Asia. *Scientific Reports*, *7*, 13717. https://doi.org/10.1038/s41598-017-14256-5

Salerno, F., Guyennon, N., Thakuri, S., Viviano, G., Romano, E., Vuillermoz, E., et al. (2015). Weak precipitation, warm winters and springs impact glaciers of south slopes of Mt. Everest (central Himalaya) in the last 2 decades (1994–2013). *The Cryosphere*, *9*, 1229–1247. https://doi.org/10.5194/tc-9-1229-2015

Shea, J. M., Wagnon, P., Immerzeel, W. W., Biron, R., Brun, F., & Pellicciotti, F. (2015). A comparative high-altitude meteorological analysis from three catchments in the Nepalese Himalaya. *International Journal of Water Resources Development*, *31*, 174–200. https://doi.org/10.1080/07900627.2015.1020417

Shrestha, D., Singh, P., & Nakamura, K. (2012). Spatiotemporal variation of rainfall over the central Himalayan region revealed by TRMM Precipitation Radar. *Journal of Geophysical Research*, *117*, D22106. https://doi.org/10.1029/2012JD018140

Steiner, J. F., Litt, M., Stigter, E. E., Shea, J., Bierkens, M. F. P., & Immerzeel, W. W. (2018). The importance of turbulent fluxes in the surface energy balance of a debris-covered glacier in the Himalayas. *Frontiers of Earth Science*, *6*, 144. https://doi.org/10.3389/feart.2018.00144

Sunako, S., Fujita, K., Sakai, A., & Kayastha, R. B. (2019). Mass balance of Trambau glacier, Rolwaling region, Nepal Himalaya: In-situ observations, long-term reconstruction and mass-balance sensitivity. *Journal of Glaciology*, *65*, 605–616. https://doi.org/10.1017/jog.2019.37

Tan, J., Huffman, G. J., Bolvin, D. T., & Nelkin, E. J. (2019). Diurnal cycle of IMERG V06 precipitation. *Geophysical Research Letters*, *46*, 13584–13592. https://doi.org/10.1029/2019GL085395

Terao, T., Islam, M. N., Hayashi, T., & Oka, T. (2006). Nocturnal jet and its effects on early morning rainfall peak over northeastern Bangladesh during the summer monsoon season. *Geophysical Research Letters*, *33*, L18806. https://doi.org/10.1029/2006GL026156

Terao, T., Murata, F., Yamane, Y., Kiguchi, M., Fukushima, A., Tanoue, M., et al. (2017). Direct validation of TRMM/PR near surface rain over the northeastern Indian subcontinent using a tipping bucket raingauge network. *SOLA*, *13*, 157–162. https://doi.org/10.2151/sola.2017-029

Ueno, K., Kayastha, R. B., Chitrakar, M. R., Bajracharya, O. R., Pokhrel, A. P., Fujinami, H., et al. (2001). Meteorological observations during 1994–2000 at the automatic weather station (GEN-AWS) in Khumbu region, Nepal Himalayas. *Bulletin of Glaciological Research*, *18*, 23–30.

Ueno, K., Toyotsu, K., Bertolani, L., & Tartari, G. (2008). Stepwise onset of monsoon weather observed in the Nepal Himalaya. *Monthly Weather Review*, *136*, 2507–2522. https://doi.org/10.1175/2007MWR2298.1

Van de Wiel, B. J. H., Moene, A. F., Steeneveld, G. J., Baas, P., Bosveld, F. C., & Holtslag, A. A. M. (2010). A conceptual view on inertial oscillations and nocturnal low-level jets. *Journal of the Atmospheric Sciences*, *67*, 2679–2689. https://doi.org/10.1175/2010JAS3289.1

Wilks, D. N. (2011). Chapter 15: Cluster analysis. In *Statistical methods in the atmospheric sciences* (3rd ed., pp. 603–616). Oxford: Academic Press. https://doi.org/10.1016/b978-0-12-385022-5.00015-4

Yamamoto, M., Ueno, K., & Nakamura, K. (2011). Comparison of satellite precipitation products with rain gauge data for the Khumb Region, Nepal Himalayas. *Journal of the Meteorological Society of Japan*, *89*, 597–610. https://doi.org/10.2151/jmsj.2011-601

Yamamoto, M. K., Shige, S., Yu, C., & Cheng, L. (2017). Further improvement of the heavy orographic rainfall retrievals in the GSMaP algorithm for microwave radiometers. *Journal of Applied Meteorology and Climatology*, *56*, 2607–2619. https://doi.org/10.1175/JAMC-D-16-0332.1

Yang, K., Guyennon, N., Ouyang, L., Tian, L. D., Tartari, G., & Salerno, F. (2018). Impact of summer monsoon on the elevation-dependence of meteorological variables in the south of central Himalaya. *International Journal of Climatology*, *38*, 1748–1759. https://doi.org/10.1002/joc.5293

Journal of Geophysical Research: Atmospheres

Supporting Information for

Twice-daily monsoon precipitation maxima in the Himalayas driven by land surface effects

Hatsuki Fujinami[1], Koji Fujita[2], Nobuhiro Takahashi[1], Tomonori Sato[3],

Hironari Kanamori[1], Sojiro Sunako[2*] and Rijan B. Kayashtha[4]

[1]Institute for Space-Earth Environmental Research, Nagoya University, Nagoya, Japan

[2]Graduate School of Environmental Studies, Nagoya University, Nagoya, Japan

[3]Faculty of Environmental Earth Science, Hokkaido University, Sapporo, Japan

[4]School of Science, Kathmandu University, Dhulikhel, Nepal

Present address: [*]Snow and Ice Research Center, National Research Institute for Earth Science and Disaster Resilience, Nagaoka, Japan

Contents of this file

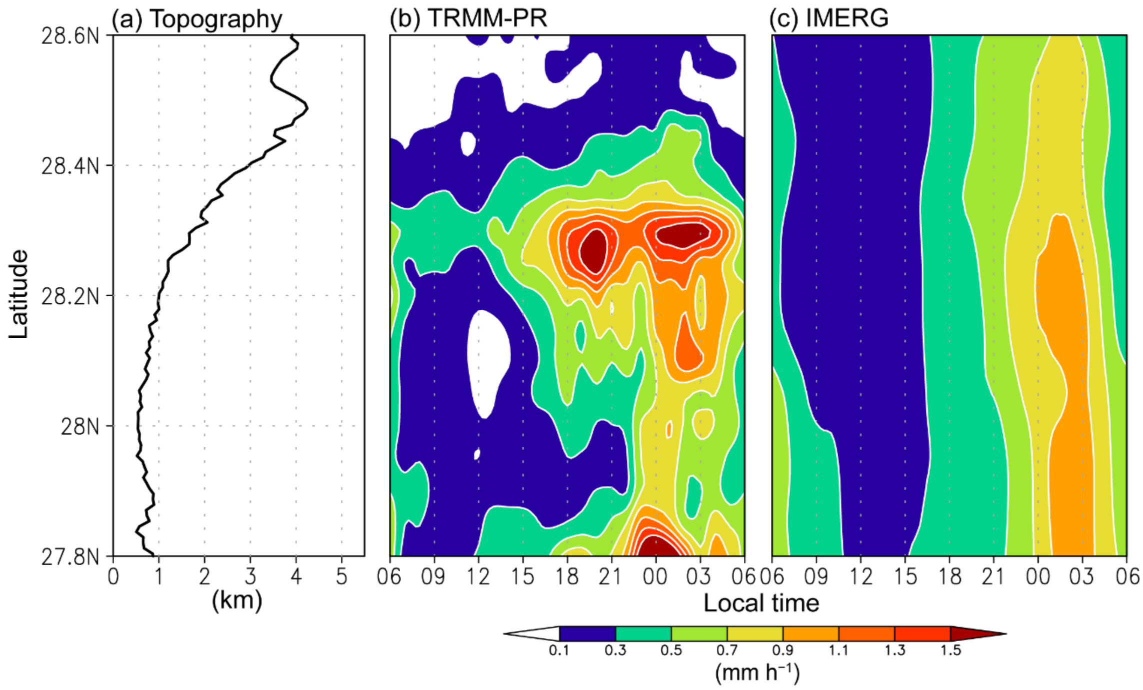

Figure S1. (a) Mean surface elevation averaged over 84.2°E–84.4°E in Marshandi River Valley where the rain gauge network was located (Barros et al., 2000). (b) Latitude–local time cross-section of precipitation (shading, mm h^{-1}) in the Marshandi River Valley from TRMM-PR hourly climatology. (c) As in (b) but for IMERG 30-minute climatology.

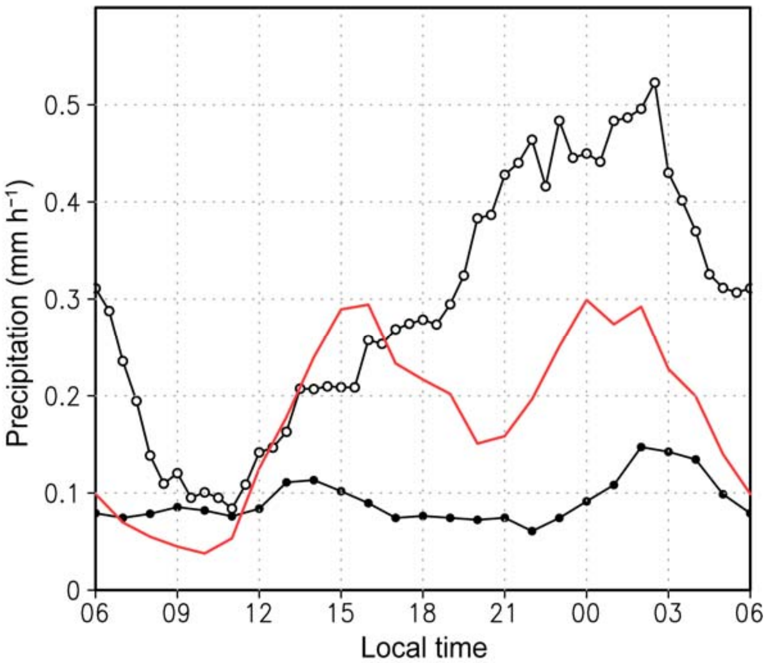

Figure S2. Diurnal cycles of precipitation in TRMM-PR diurnal climatology (solid line with closed circles) and IMERG diurnal climatology (solid line with open circles) around the Rolwaling AWS (27.84°N, 86.49°E). The solid red line represents the diurnal precipitation cycle at Rolwaling AWS as in Figure 4a. The values in TRMM-PR are averaged over a 0.1° × 0.1° rectangular grid centered on 27.85°N, 86.5°E, and the values in IMERG are based on a grid-point at 27.85°N, 86.45°E.